High-speed atomic force microscopy coming of age

2012 Nanotechnology 23 062001

(http://iopscience.iop.org/0957-4484/23/6/062001)

Nanotechnology **23** (2012) 062001 (27pp) doi:10.1088/0957-4484/23/6/062001

TOPICAL REVIEW

High-speed atomic force microscopy coming of age

Toshio Ando

Department of Physics and Bio-AFM Frontier Research Center, Kanazawa University, Kakuma-machi, Kanazawa 920-1192, Japan

Received 18 August 2011, in final form 9 November 2011
Published 17 January 2012
Online at stacks.iop.org/Nano/23/062001

Abstract
High-speed atomic force microscopy (HS-AFM) is now materialized. It allows direct visualization of dynamic structural changes and dynamic processes of functioning biological molecules in physiological solutions, at high spatiotemporal resolution. Dynamic molecular events unselectively appear in detail in an AFM movie, facilitating our understanding of how biological molecules operate to function. This review describes a historical overview of technical development towards HS-AFM, summarizes elementary devices and techniques used in the current HS-AFM, and then highlights recent imaging studies. Finally, future challenges of HS-AFM studies are briefly discussed.

S Online supplementary data available from stacks.iop.org/Nano/23/062001/mmedia

(Some figures may appear in colour only in the online journal)

1. Introduction

A vast array of studies have long been performed by various approaches to understand how proteins work. The recent technical innovation in protein studies is brought about by single-molecule fluorescence microscopy created in the early 1990s [1, 2]. The dynamic behavior of individual protein molecules at work can be examined by the observation of the dynamic behavior of fluorescent spots, each being emitted from a fluorophore attached to a selected locus of the molecule. By this innovation, the depth of our understanding of how proteins function has become incomparable with the past. Nevertheless, an insufficiency in our understanding is obvious. This is mainly because we still have technical limitations. Protein molecules themselves are invisible in the fluorescence observations even when super-resolution fluorescence microscopy [3] is used. The structure of biological molecules has been studied using x-ray crystallography, NMR, electron microscopy and atomic force microscopy (AFM) but the obtained structures are essentially static. Thus, the concomitant assessment of structure and dynamics is infeasible. Even the emerging x-ray free-electron laser [4] will not break this limitation. To overcome this long-standing problem prevailing protein research and make it possible to simultaneously record the structure and dynamics of biological molecules, high-speed AFM has been developed in the last two decades [5, 6] and is now coming of age [7].

After the advent of AFM in 1986 [8], its potential capabilities as a novel tool in biological research have been actively explored in pioneering works [9–11]. In life sciences, AFM is now routinely used as a nanotool for various measurements under physiological solution environments [12, 13]; high-resolution imaging of biological samples [14–16], recognition and localization of specific molecules [17, 18] as well as force measurements to estimate the strength of intra- and intermolecular bonds at the single-molecule level [19–21] and the elasticity of biological surfaces [22, 23]. This remarkable progress has been basically supported by reinforcement of the initial configuration of an AFM apparatus with newly developed devices and techniques such as microfabricated cantilevers [24], the optical lever method for cantilever deflection detection [25] and the tapping mode [26]. The microfabricated cantilevers and the optical lever method simplified the AFM apparatus and its operation (figure 1). In the tapping mode, the cantilever tip is vertically oscillated at the first resonant frequency of the cantilever

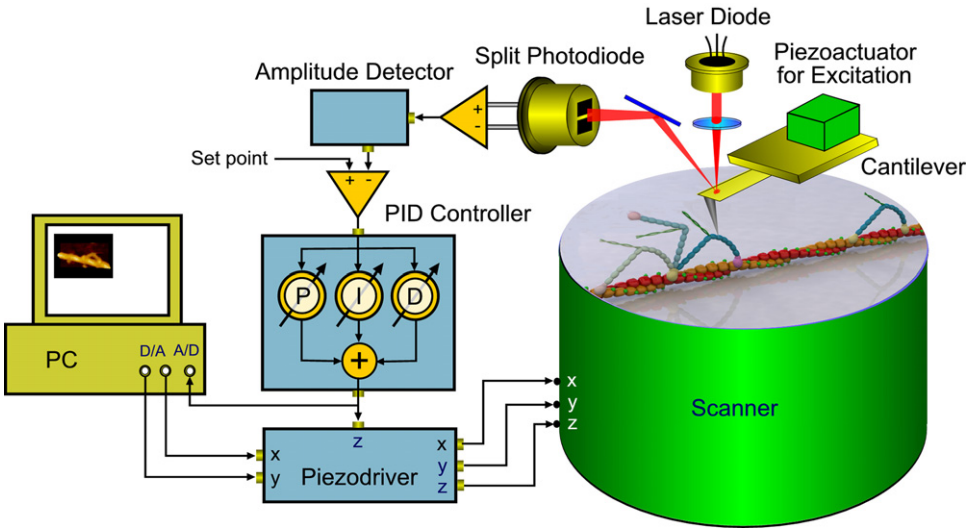

Figure 1. Schematic presentation of tapping mode AFM system.

and brought into periodic contact with the sample surface. Hence, the tapping mode significantly reduces the frictional force exerting from the cantilever tip to the sample during the raster scanning of the sample. In the previous contact mode, biological samples weakly attached to a substrate surface are easily swept away by the cantilever tip.

In the early stage when pioneering studies of bio-AFM imaging were being carried out, several groups attempted to observe dynamic biological events. Hansma and colleagues observed at 1 min intervals the clotting process by fibrin which was initiated by the digestion of fibrinogen with thrombin [11]. A group including one of the inventors of AFM (i.e. Binnig) also attempted to image the dynamic processes of live cells being infected by virus [27] and binding of antibody to the S-layer [28]. After the introduction of the tapping mode, DNA-involved dynamic processes were studied by Hansma's group and Bustamante's group; DNA digestion by DNAase [29] binding of RNA polymerase to DNA [30], transcription process [31] and diffusion of RNA polymerase along DNA strands [32]. Other types of dynamic processes studied were digestion of collagen I by collagenase [33] and closing of nuclear pores upon exposure to 5% CO_2 [34]. The imaging rate used in these studies was very low as a matter of course. Even in the fastest imaging, it was ∼2 frames min^{-1}. Therefore, no clear images were acquired for rapidly moving molecules and their time-lapse images could not well resolve the dynamic processes. To circumvent the low imaging rate, Radmacher measured height fluctuations (∼1 nm) at a top-surface locus of lysozyme which specifically occurred when the enzyme was digesting oligoglycosides [35]. A similar study was carried out with urease and ∼1 nm height fluctuations of 100–200 Hz were detected [36].

Looking back these early studies, it is obvious that AFM was expected to play a role in visualizing dynamic biological processes at high spatial resolution because AFM is only the method capable of directly visualizing vital biological samples in aqueous solutions. However, this expectation could not be met by the low imaging rate. As mentioned above, rather than AFM, single-molecule fluorescence microscopy created in the early 1990s has been much more successful in observing dynamic biomolecular processes, although the observation is performed in an indirect way.

As will be described later, efforts towards increasing the imaging rate of AFM have been carried out since the early 1990s. Through steady efforts for two decades, high-speed AFM has now materialized. In fact, several biomolecular processes have recently been captured clearly, and the number of publications on high-speed AFM imaging has rapidly increased in the last 2 years. In this review, a historical overview of technical developments towards high-speed AFM is first described, which is followed by theoretical considerations for the imaging rate and descriptions of elementary devices and techniques specialized for high-speed AFM. Then, recent studies of high-speed AFM imaging are highlighted. This review is concluded by the discussion of future challenges to be met in order to expand the scope of high-speed AFM applications in biological research. More comprehensive descriptions of high-speed AFM instrumentation are given elsewhere [7]. Details of the historical overviews of bio-AFM development and application are also given elsewhere [37, 38].

2. History of high-speed AFM development

2.1. Initial stage

In the early 1990s, only a few years after the invention of AFM, Calvin Quate and colleagues initiated the development of high-speed AFM [39]. Quate, one of the inventors of AFM, aimed at fast inspection and lithography of a wide area of hard material surfaces using AFM. To this end, they developed cantilevers and cantilever arrays with integrated sensors and/or actuators using MEMS technology [40–44]. The self-sensing and self-actuation capabilities significantly simplified the configuration of AFM set-up. However, the

fabrication of these cantilevers was only possible in relatively large dimensions, resulting in low resonant frequencies and large spring constants. Insulation coating of the integrated cantilevers for the use in liquids further lowered the resonant frequency [45]. This approach, therefore, did not extend to high-speed AFM for biological research. Nevertheless, their intention of increasing the scan speed of AFM was taken over by Hansma and Ando.

Hansma's group and my group employed the same approach, i.e. increasing the feedback bandwidth by developing fast-response devices. Both groups developed small cantilevers [6, 46, 47] and optical beam deflection (OBD) detectors for small cantilevers [6, 48]. My group additionally developed a fast scanner and a fast amplitude detector [6]. Hansma's group reported imaging of DNA at 0.6 frames s^{-1} (fps) [49] and dynamic association/dissociation between GroES and GroEL [5]. However, the feedback bandwidth was not high enough and therefore the molecular events were recorded by scanning the sample stage only in the x and z directions. A more complete high-speed AFM system was reported by my group in 2001 and 2002 [6, 50], which enabled filming of the Brownian motion of myosin V on mica surfaces at 12.5 fps [6]. However, the feedback bandwidth was not high enough to have a capability of low invasiveness to fragile proteins. The period from the early 1990s through 2002 is considered to be the initial stage of high-speed AFM development.

2.2. Second stage

In the second stage from 2003–2007, further efforts were carried out. A notable improvement was achieved by the invention of an active damping technique for the z-scanner [51] and a dynamic proportional–integral-derivative controller [52]. Further smaller cantilevers with a resonant frequency of 1.2 MHz in water and a small spring constant of ∼0.2 N m^{-1} were developed by Olympus. As a result, the feedback bandwidth was significantly increased up to ∼100 kHz. Fast phase imaging was also achieved by the development of a fast phase detector capable of detecting the phase signal every oscillation cycle of a cantilever [53]. In 2008, my group finalized the development of high-speed AFM suitable for observing dynamic structural changes of biological molecules [7]. Since then, my group has been shifting our efforts towards applying the finalized high-speed AFM instrument to the study of proteins and developing the next generation of high-speed AFM applicable to live cells. Hansma's group developed fast data acquisition systems [54, 55] and high-speed scanners with a relatively large scan range (6–15 μm in x and y directions and 6 μm in the z direction) [55, 56]. Miles' group developed a resonant x-scanner using a tuning fork with resonant frequencies of 30–100 kHz [57] and a fast digital processing system for acquiring cantilever deflection data [58], and demonstrated ultrafast imaging (1300 fps) of collagen fibers in an ambient environment [58]. This remarkable speed was, however, achieved in the constant-height mode (without feedback scan of the z-scanner). Their high-speed AFM is therefore only applicable to samples firmly attached to a substratum in an ambient environment or to very stable non-biological samples in liquids. It is notable that, in this developmental stage, researchers of control engineering participated in developing fast positioning techniques for AFM using more sophisticated control techniques. However, the complicated control techniques can only be implemented with slow digital circuits. Schitter, one of the previous collaborators of Hansma, is now trying to implement sophisticated control schemes into emerging field programmable analog array (FPAA) circuits [59].

2.3. Current stage

After the second stage, the number of users of the high-speed AFM apparatus designed by my group is rapidly increasing. Consequently, a relatively wide range of application studies are now being carried out. Regarding the technical development of high-speed AFM, a wide-area and high-speed scan capability is being pursued. However, the feedback bandwidth seems to have already reached the maximum possible level (∼100 kHz) as far as the configuration of the AFM set-up similar to previous ones is used (i.e. tapping mode, piezoactuator-based sample-stage scanner, small cantilevers and OBD detection of cantilever deflection). Rather than attempting to further increase the scan speed, functional augmentation to high-speed AFM is now being pursued and bringing a new modality of bio-imaging which will be briefly described in section 6.

3. Theoretical basis for feedback bandwidth and imaging rate

Here, factors limiting the scan speed of tapping mode AFM are quantitatively described. It will be shown that the highest possible imaging rate R_{max} is determined by the bandwidth of feedback control to maintain the tapping force constant during scanning as well as by scan parameters and the sample itself.

3.1. Highest possible imaging rate

When a sample is scanned over an area of $W \times W$ with scan velocity V_s in the x direction and N scan lines in the y direction, the image acquisition rate R is given by $R = V_s/(2WN)$. Supposing that the sample surface corrugation is characterized with a single spatial frequency ν in the x direction, then the feedback scan is executed in the z direction with frequency $f = \nu V_s$ to trace the sample surface.

The bandwidth f_B of the closed feedback loop should be equal to or higher than f, and thus we obtain the relationship $R \leq f_B/(2\nu WN)$. The feedback bandwidth f_B is usually defined by a feedback frequency f at which a closed-loop phase delay of $\pi/4$ occurs in tracing the sample surface. The phase delay in the closed loop (φ_{closed}) is approximately twice that in the open loop (φ_{open}), provided the feedback gain is maintained at ∼1 [7]. The phase delay is caused by the limited response speed of devices contained in the feedback loop and by the time delay due to a 'parachuting' effect mentioned below. By denoting the total time delay by $\Delta\tau_{total}$, φ_{open} is given by $\varphi_{open} = 2\pi f \Delta\tau_{total}$. The phase delay

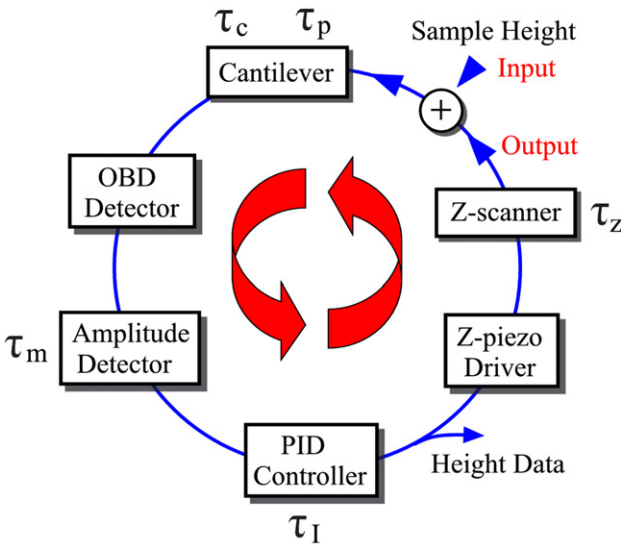

Figure 2. Feedback loop of tapping mode AFM and main time delays. The input to the feedback loop is the variation of sample surface height and the output is the displacement of the z-scanner. The time delay in the loop is mainly produced by the cantilever response time (τ_c), the parachuting time (τ_p), the time required to measure the cantilever oscillation amplitude (τ_m), the integral time of error signal at the PID controller (τ_I) and the z-scanner response time (τ_z).

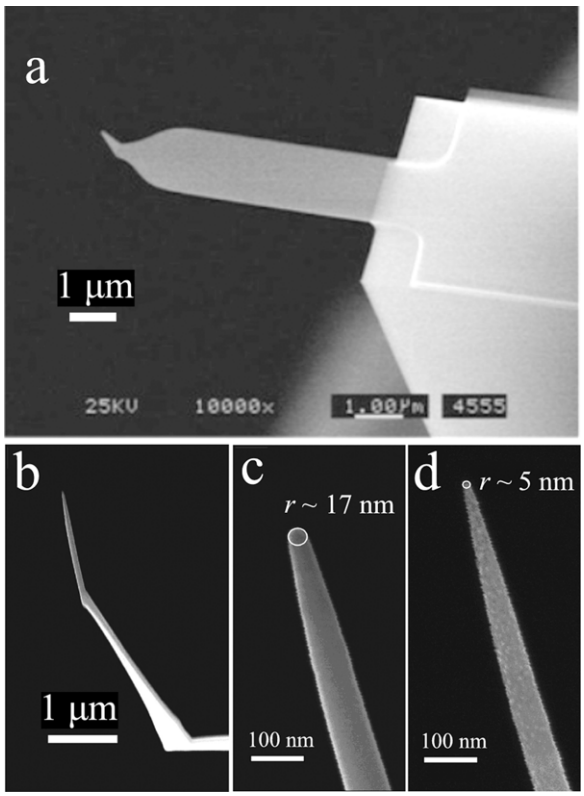

Figure 3. Small cantilever and EBD tip. (a) SEM image of a small cantilever. (b)–(d) SEM images of EBD tips. The apex radius of the tip formed by EBD is not small (c) but can be reduced by nitrogen or oxygen plasma etching to 4–5 nm (d).

can be compensated by a factor of α using the (P + D) operation of the PID feedback controller. f_B is thus given by $f_B = \alpha/(16\Delta\tau_{total})$. Hence, the highest possible imaging rate is given by $R_{max} = \alpha/(32\nu WN\Delta\tau_{total})$, when the sample fragility is not taken into account. To materialize, for example, $R_{max} = 25$ fps for $\alpha = 2.5$, $\nu = 0.1$ nm^{-1}, $W = 200$ nm and $N = 100$, we have to achieve $f_B = 100$ kHz and thus $\Delta\tau_{total} = 1.6$ μs.

3.2. Time delay

In the closed feedback loop, there are several devices with certain time delays to response (figure 2). The main time delays are as follows; (1) the response time of an oscillating cantilever, (2) the time required for measuring the cantilever oscillation amplitude, (3) the time of integrating the error signal with a feedback controller, (4) the response time of the z-scanner and (5) the 'parachuting' time mentioned below.

When a cantilever tip taps a sample surface, a brief stepwise force is exerted on the cantilever. The cantilever responds to this stepwise force with a response time given by $\tau_c = Q_c/(\pi f_c)$, where Q_c and f_c are the cantilever's quality factor and the first resonant frequency in an aqueous solution, respectively. The minimum time required for measuring the cantilever oscillation amplitude τ_m is given by $\tau_m = 1/(2f_c)$. The z-scanner is driven at a feedback frequency f. The response of the z-scanner with the first resonant frequency f_z and a quality factor Q_z is characterized with a second-order transfer function. The phase delay φ_z at the feedback frequency f is estimated from the phase–frequency relationship (i.e. the Bode phase plot) of the transfer function. The time delay τ_z is given by $\tau_z = \varphi_z/(2\pi f)$. A previous argument as to τ_z is based on an assumption that the z-scanner is driven stepwise [7] but this assumption is not practical because the z-scanner is driven by the output signal from an analog feedback controller through the z-piezodriver. The integral time of error signal with a feedback controller τ_I cannot be expressed explicitly but was previously given through a theoretical consideration and experimental measurements [7]. It is approximately expressed by $\tau_I = 4h_0 \sin(\varphi_{closed}/2)/(A_0 f_c)$, where h_0 is the sample height and A_0 is the free oscillation amplitude of the cantilever.

When the cantilever encounters a steeply inclined region of the sample, the tip completely detaches from the sample surface and time elapses until it lands on the surface again (i.e. parachuting). The parachuting time is prolonged when the amplitude set point A_s to be maintained constant during scanning is set close to the free oscillation amplitude A_0. This is because the error signal $(A_0 - A_s)$ to be integrated by a feedback controller is saturated at a small value during parachuting [7, 52]. An approximate analytical expression for the parachuting time τ_p was previously given to be $\tau_p = [(\tan\beta)/\beta - 1]/f_c$, where β is given by $\beta = \cos^{-1}[(A_0 - A_s)/\{5h_0 \sin(\varphi_{closed}/2)\}]$ [7].

4. Instrumentation of high-speed AFM

In the high-speed AFM apparatus we developed, all the time delays mentioned above are minimized. This apparatus is now commercially available from Research Institute of Biomolecule Metrology (RIBM), Co., Ltd (Tsukuba,

Japan). Here, devices with minimized time delays are briefly described.

4.1. Small cantilevers, OBD detector and amplitude detector

Several types of small rectangular cantilevers made of silicon nitride have been developed by Olympus collaborating with my group [6, 60]. The highest end cantilevers have dimensions of 6 μm long, 2 μm wide and 90 nm thick (figure 3(a)). The resonant frequencies are 3.5 MHz in air and 1.2 MHz in water. The spring constant is 0.2 N m^{-1} and the quality factor in water is ∼2. Therefore, the response time in water is ∼0.5 μs. A slightly larger type (BioLever fast BL-AC10DS-A2, Olympus; 9 μm long, 2 μm wide and 130 nm thick; resonant frequencies 1.5 MHz in air and 0.6 MHz in water; spring constant ∼0.1 N m^{-1}) is commercially available from Olympus (Tokyo, Japan), Atomic Force F&E GmbH (Mannheim, Germany), Bruker (CA, USA) and Asylum Research (CA, USA). Although not yet commercialized, small cantilevers will soon also be available from NanoWorld AG (Neuchâtel, Switzerland). The change in the angle $\Delta\varphi$ of a cantilever's free end is given by $3\Delta z/2L$, where Δz is the displacement of the free end and L is the length of the cantilever. Therefore, for the deflection detection of small cantilevers, angle-based OBD detectors are advantageous compared with distance-based detectors. The shorter cantilevers give 10–20 times higher sensitivity to an OBD detector than conventional cantilevers.

The tip of the small cantilevers manufactured by Olympus has a bird-beak-like shape with an apex radius of 15–24 nm. Small cantilevers with a sharper tip made by electron beam deposition (EBD) are also available as an option. When a scanning electron microscope (SEM; a low vacuum type is ideal) is available, EBD tips can be easily grown under an atmosphere of phenol gas sublimated from phenol crystals (figures 3(b) and (c)). They grow at ∼1 μm min^{-1} under a low vacuum condition. The tip can be sharpened by nitrogen or oxygen plasma etching (figure 3(d)). The apex radius can be reduced usually to ∼4 and to ∼0.5 nm in the best case.

In the OBD detector (figure 4), a 20× objective lens with a long working distance of 24 mm (SLWD 20×, Nikon) is used to focus a laser beam onto a small cantilever [6]. This lens is also used to collect a laser reflected back from the cantilever and to view the cantilever and sample stage under an optical microscope. The incident and reflected laser beams are separated using a quarter-wavelength plate and a polarization beamsplitter.

The oscillation amplitude of a cantilever is measured by a peak-hold method at every half-cycle of oscillation (i.e. $\tau_m = 1/(2f_c)$) [6] or by a Fourier method at every cycle of oscillation (i.e. $\tau_m = 1/f_c$) [7]. In the former method, the peak and bottom voltages of a sinusoidal signal output from the split photosensor of the OBD detector are held by sample/hold circuits, and their difference is output as a peak-to-peak amplitude signal. Since only two-point voltages are used, it is susceptible to the effect of thermal fluctuations of a cantilever. The latter method uses almost all the signals within one oscillation cycle and hence is much less susceptible to the thermal effect.

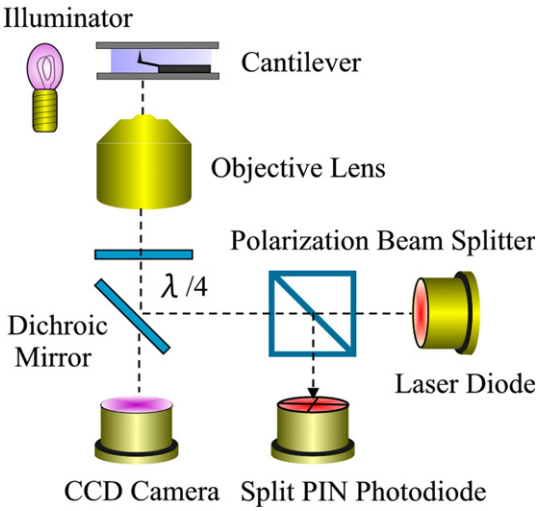

Figure 4. Schematic presentation of objective lens type of OBD detection system. The collimated laser beam is reflected up by the dichroic mirror and incident on the objective lens. The beam reflected back from the cantilever is collimated by the objective lens, separated from the incident beam by the polarization beamsplitter and $\lambda/4$-wave plate, and reflected onto the split photodiode. The objective lens is also used to view the cantilever, the focused laser spot and the sample stage through the CCD camera.

4.2. Sample-stage scanner and active damping of z-scanner

To design a sample-stage scanner to be driven at high frequencies, we have to consider various factors; not only the scanner's resonant frequency and unwanted vibrations but also hydrodynamic pressure. Quick displacement of a sample stage in the z-direction produces high hydrodynamic pressure, which tends to move the cantilever chip as well as the cantilever holder since they are located close to the sample stage [50]. This movement results in a considerable time delay in the cantilever response. Therefore, we use a small sample stage 1–2 mm in diameter. In addition, the laterally overlapped region of the sample stage and the cantilever is minimized. This means that only areas near the edge region of the sample stage are imaged [61].

Among the x-, y- and z-scanners, the z-scanner is displaced at the highest frequency. This high-frequency displacement produces a large impulsive force to its supporting mechanism, which is apt to cause unwanted vibrations of the z-scanner. To counteract the impulsive force and thereby minimize vibrations, two identical piezoactuators are placed at a supporting base in the opposite direction and displaced simultaneously with the same length [6, 7, 50, 62]. An alternative method we have recently employed is to hold a piezoactuator at its four rims parallel to the displacement direction so that the center of mass of the piezoactuator is not displaced [63]. In the former method, the resonant frequency and the maximum displacement are ∼170 kHz and 2 μm, respectively, while in the latter method they are ∼370 kHz and 1 μm, respectively. In the x-scanner with the maximum displacement of ∼2 μm, a piezoactuator is held at both ends with flexures so that its center of mass is unchanged during scanning [7]. The slowest y-scanner displaces a block of the

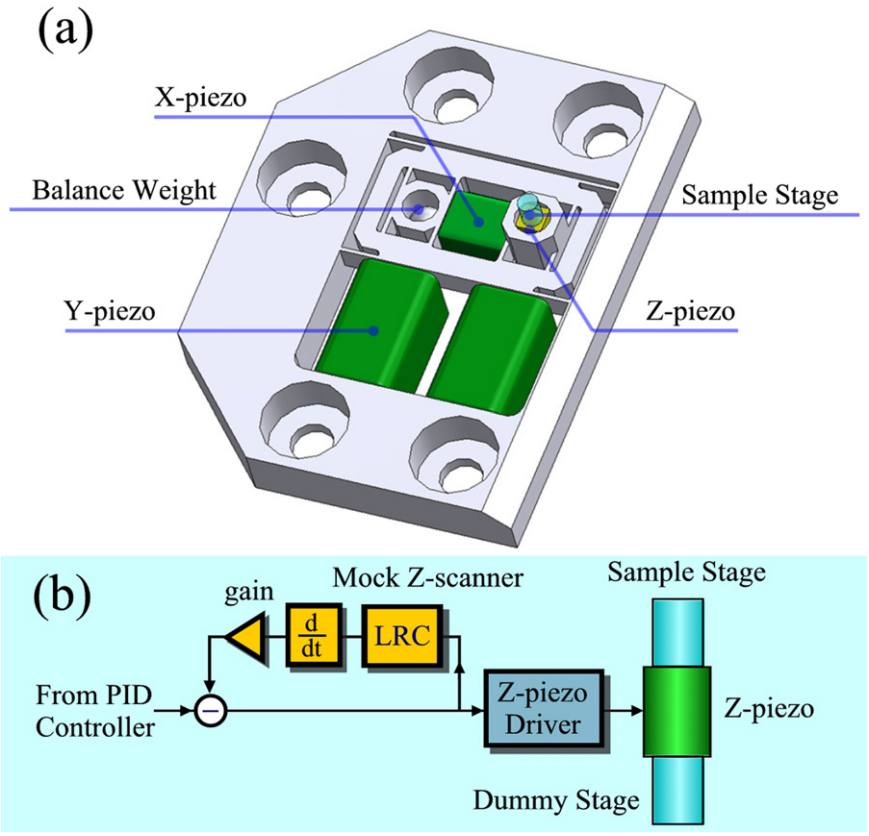

Figure 5. High-speed scanner and active damping. (a) Sketch of high-speed scanner. A sample stage (glass rod) is glued on the top surface of the z-piezoactuator using nail enamel (a dummy stage attached to the bottom surface of the z-piezoactuator is hidden). The z-piezoactuator is held at the four rims parallel to the displacement direction. The dimensions ($W \times L \times H$) of the z-piezoactuator are $3 \times 3 \times 2$ mm^3. The gaps in the supporting base are filled with an elastomer for passive damping. (b) Active damping of z-scanner vibrations. The *LRC* circuit (mock z-scanner) is constructed so that its transfer function is similar to that of the real z-scanner.

x- and z-scanners, the x-scanner displaces a block of the z-scanner and the z-scanner displaces a glass-rod sample stage (figure 5(a)).

To damp z-scanner vibrations, we developed an active damping technique based on a Q-control method with a 'mock z-scanner' [51]. In a conventional Q-control method [64, 65], the displacement or velocity (V_z) of the z-scanner has to be measured and a signal proportional to $-V_z$ is added to the signal to be input to the z-piezodriver (i.e. output from a feedback controller). However, it is difficult to measure the displacement or velocity. In our method, the mock z-scanner (an *LRC* circuit) characterized with a transfer function similar to that of the real z-scanner is used (figure 5(b)). An input signal to the z-piezodriver is also input to the mock z-scanner and the output from the mock z-scanner is used for Q-control (i.e. its minus derivative is added to the output signal from a feedback controller). As a result, the quality factor Q_z is reduced to 1–2. Although it is possible to further reduce Q_z down to 0.5, we do not do so because the smaller Q_z results in a larger phase delay and also because the first resonance at 370 kHz would not be excited by a feedback signal with a frequency of ∼100 kHz. The time delay of the z-scanner is ∼0.36 μs for 100 kHz driving.

4.3. Feedback controller and drift compensator

It is difficult to make high-speed imaging compatible with low invasive imaging. In order for the oscillating cantilever tip to tap the sample surface with a small force, the amplitude set point has to be set very close to the free oscillation amplitude. As already mentioned, this condition promotes tip-parachuting and prolongs its duration. We solved this problem by devising a new PID controller (named a dynamic PID controller) with a capability to automatically change the PID's gain parameters, depending on the cantilever oscillation amplitude [52]. When the amplitude exceeds a threshold level (set at the amplitude set point or slightly above), the gains are increased. The oscillation amplitude thereby quickly returns towards the set point before the error signal is saturated. Consequently, the feedback bandwidth becomes independent of the set point as long as the set point is smaller than 0.9–0.95.

When a piezoactuator is driven continuously for a long time, its temperature is increased. As a result, the extension coefficient of the piezoactuator is usually lowered to some extent. In the tapping mode, a cantilever is continuously excited by a sinusoidally oscillated piezoactuator placed at the cantilever holder. The cantilever free oscillation amplitude

A_0 gradually declines by the thermal effect. When A_0 is set at 1 nm and the set point A_s is set at $0.9A_0$ (these values are routinely used for imaging delicate biological samples), their difference is only 0.1 nm. Under this condition, the downward drift of A_0 easily leads to complete dissociation of the cantilever tip from the sample surface because the feedback system misinterprets the change in the cantilever oscillation amplitude and hence withdraws the sample stage from the cantilever tip. Thus, to achieve stable imaging under a small tapping force, A_0 has to be kept constant precisely. However, there is no way to measure A_0 during successive imaging. Instead of measuring A_0, we measure the second harmonic oscillation amplitude A_{2nd} which is sensitive to the tip–sample interaction [52, 66]. A_{2nd} is maintained constant by changing the cantilever excitation power using a slow feedback control [52]. This compensation method allows very stable imaging under a small tapping force.

5. High-speed AFM imaging

As shown in table 1, from 2001–2008 the number of publications on high-speed AFM imaging gradually increased, and sharply increased in the most recent 2 years. This leap reflects the recent maturity of the high-speed AFM technique and the increase in the number of users. A prototype of a high-speed AFM apparatus began to be commercially available from RIBM around 2006. In 2008 an international consortium of high-speed bio-AFM was founded by the cooperation of six laboratories throughout the world. These laboratories are using the highest-end high-speed AFM instruments designed by my group.

5.1. Early studies

Even in the period when the development of high-speed AFM instruments was going on, a few groups carried out high-speed bio-imaging experiments using the test and prototypic apparatuses. Through imaging experiments, my group examined the capability of test apparatuses to find instrumental problems to improve. For example, visualization of the following biomolecular processes was attempted; calcium-induced dissociation of calmodulin (CaM) from the neck regions of myosin V (M5) [67], gliding movement of actin filaments over a myosin-coated surface (movie S1 available at stacks.iop.org/Nano/23/062001/mmedia) [62], conformational change of single-headed dynein C hydrolyzing ATP [62], kinesin movement along microtubules [67] and association/dissociation between GroES and GroEL under the control of the GroEL ATPase cycle [62]. It is noteworthy that flash photolysis of caged compounds was introduced for the first time to AFM imaging [62, 67]. This technique is well matched with high-speed AFM when transient events triggered by the release of ligands are visualized. It was used to observe CaM dissociation from M5 upon Ca^{2+} release and GroES binding to GroES upon ATP release (movie S2 available at stacks.iop.org/Nano/23/062001/mmedia) [62, 67]. Even in these early trials, dynamic biomolecular events were successfully captured but fragile samples such as microtubules were often broken during imaging. Torimitsu's group imaged the complex of biotinylated DNA and streptavidin but the complex was disrupted during imaging [75]. Using a feedback-control-free high-speed AFM apparatus developed by Miles' group [57], Hobbs' group imaged growing polyethylene oxide films at 14 fps but the resolution was low [68]. Takeyasu's group successfully observed the opening and closing of the apical region of GroEL during the ATPase reaction as well as the dynamic interaction between GroEL and GroES [70]. However, in this study (as well as in the previous study mentioned above [62]), GroEL was placed on a mica surface in an end-up orientation, so that one of the two rings was invisible and inaccessible to GroES. Therefore, the postulated [120] but controversial [121] asymmetric conformational changes in the double-ring structure and the resulting asymmetric binding of GroES could not be examined. This experimental restriction was removed later by the preparation of an appropriate substrate surface [82, 93].

Among various imaging studies carried out in this stage, the dynamic visualization of *Eco*P15I–DNA complex performed by Takeyasu and collaborators [74] is notable. *Eco*P15I is a type III restriction–modification enzyme with a low ATPase activity. The establishment of the endonuclease activity requires complex formation by the two molecules bound to unmethylated and inversely oriented specific non-palindromic recognition sites (i.e. 5′-CAGCAG—CTGCTG) which are distantly separated (up to 3.5 kb) on the same DNA molecule. Thus, it has been an interesting question how the two enzyme molecules efficiently encounter each other to overcome the distance and to cleave the DNA double strand [122]. A simple model accounting for the efficient encounter could be that the ATPase reaction by the enzyme molecules bound to the recognition sites drives translocation of the DNA double strand to extrude loops, thus efficiently leading to collision of the molecules. However, the ATPase activity is too low to explain such a long translocation [123]. The high-speed imaging showed that *Eco*P15I in fact translocated DNA in an ATP-dependent manner and consequently caused accumulation of supercoiling[1]. The enzyme bound to its recognition site also made non-specific contacts with other DNA sites, thus forming loops (diffusive looping). The loops formed were extruded by the ATPase-driven translocation of DNA. Thus, the two mechanisms (translocation and diffusive looping) effectively reduce the distance between the recognition sites. However, recent single-molecule magnetic tweezers experiments showed that a DNA double strand stretched so as not to form loops could be cleaved, suggesting that one-dimensional diffusion of an *Eco*P15I molecule is sufficient to reach a second molecule attached to its recognition site, and also that DNA cleavage occurs even when an *Eco*P15I molecule within the dimeric complex is not bound to its recognition site on the DNA [124]. A recent review discussed these and other experimental results to reconcile different models and provided suggestions for further experiments [125].

[1] See supplemental movie available at: www.pnas.org/content/suppl/2007/07/13/0700483104.DC1/0843Movie3.avi.

Table 1. Chronological progress of publications on high-speed AFM imaging.

Year	n[a]	Targets and subjects	Research group
2001	1	• Brownian motion of myosin V [6]	Ando
2002	0	None	
2003	2	• Brownian motion of myosin V [50]	Ando
		• Kinesin movement along MT &CaM dissociation from myosin V [67]	Ando
2004	0	None	
2005	3	• Actin gliding, structural change of dynein C, GroES–GroEL interaction [62]	Ando
		• Polyethylene oxide films during crystal growth [68]	Hobbs
		• Polymer films during crystallization from the melt [57]	Miles
2006	3	• MT destruction and conformational change of myosin V [69]	Ando
		• Conformational change of GroEL and GroEL–GroES interaction [70]	Takeyasu
		• DNA–nuclease interaction [71]	Takeyasu
2007	5	• Crystallization of a $CaCO_3$ thin film from supersaturated solution [72]	Miles
		• Ultrafast imaging of collagen [58]	Miles
		• Brownian motion and photodegradation of π-conjugated polyrotaxane [73]	Shinohara
		• DNA translocation and looping by type III restriction enzyme [74]	Takeyasu
		• Biotinylated DNA–streptavidin interaction [75]	Torimitsu
2008	5	• Anisotropic diffusion of point defects in streptavidin 2D crystals [76]	Ando
		• Identification of intrinsically disordered regions of proteins [77]	Ando
		• Human chromosomes in liquid [78]	Miles
		• DNA–nuclease interaction [79]	RIBM
		• Effect of Ca^{2+} on vesicle fusion [80]	Torimitsu
2009	10	• Dynamic equilibrium at the edge of bR 2D crystals [81]	Ando
		• Structural change of CaM and actin polymerization on streptavidin 2D crystals [82]	Ando
		• Unidirectional translocation of cellulase along cellulose fibers [83]	Igarashi
		• Translocation of *Eco*RII restriction enzyme along DNA [84]	Lyubchenko
		• Fabrication and imaging of hard material surface [85]	Miles
		• Purple membrane in contact mode HS-AFM [86]	Scheuring
		• Thermal motion of π-conjugated polymer chain [87]	Shinohara
		• Opening of 3D hollow structure of DNA origami [88]	Sugiyama
		• Opening of 3D hollow structure of DNA origami [89]	Sugiyama
		• ATP-induced conformational change in $P2X_4$ receptors [90]	Shinozaki
2010	21	• Walking myosin V along an actin filament [91]	Ando
		• Photo-induced structural change in bR [92]	Ando
		• 2D crystal formation of annexin A–V and height change of p97 [93]	Ando
		• Analysis of components covering magnetosome surface [94]	Ando
		• Time course of cell death by antimicrobial peptide [95]	Fantner
		• Dissolution of extreme UV exposed resist films under developing [96]	Itani
		• Dissolution of extreme UV exposed resist films under developing [97]	Itani
		• Process of forming supported planar lipid bilayer [98]	Le Grimellec
		• Self-assembly of amyloid-like fibrils [99]	Milhiet
		• Effect of ClpX on FtsZ polymerization [100]	Ogura
		• Membrane-mediated protein–protein Interaction [101]	Scheuring
		• Photodegradation of chiral helical π-conjugated polymer chain [102]	Shinohara
		• Base-excision repair of damaged DNA in DNA origami scaffold [103]	Sugiyama
		• Tension effect on DNA methylation [104]	Sugiyama
		• Formation/disruption of G-quadruplex in DNA nanoscaffold [105]	Sugiyama
		• Programmed self-assembly of DNA origami jigsaw pieces [106]	Sugiyama
		• Programmed self-assembly of DNA origami jigsaw pieces [107]	Sugiyama
		• Dissociation of histone from nucleosome [108]	Takeyasu
		• Height change of acid-sensing ion channel 1a upon acidification [109]	Takeyasu
		• Breaking of nanocapsules of DNA–azobenzene conjugate by UV light [110]	Tanaka
		• Structural change of bR trimer in a stretched membrane [111]	Torimitsu
2011 up to September 2	8	• Morphological transformation of detergent micells [112]	Ando
		• bR in response to alternating two-color illumination [113]	Ando
		• Rotary catalysis of rotorless F_1-ATPase [114]	Ando
		• Dislocation of cellulase hydrolyzing cellulose fibers [115]	Ando
		• CENP-W complexed with CENP-T [116]	Fukagawa
		• Opening of DNA cuboid [117]	Sugiyama
		• Synthetic molecular motor [118]	Turberfield
		• Ferritin adsorption onto a silicon substrate [119]	Yamamoto

[a] n represents the number of publications in respective years.

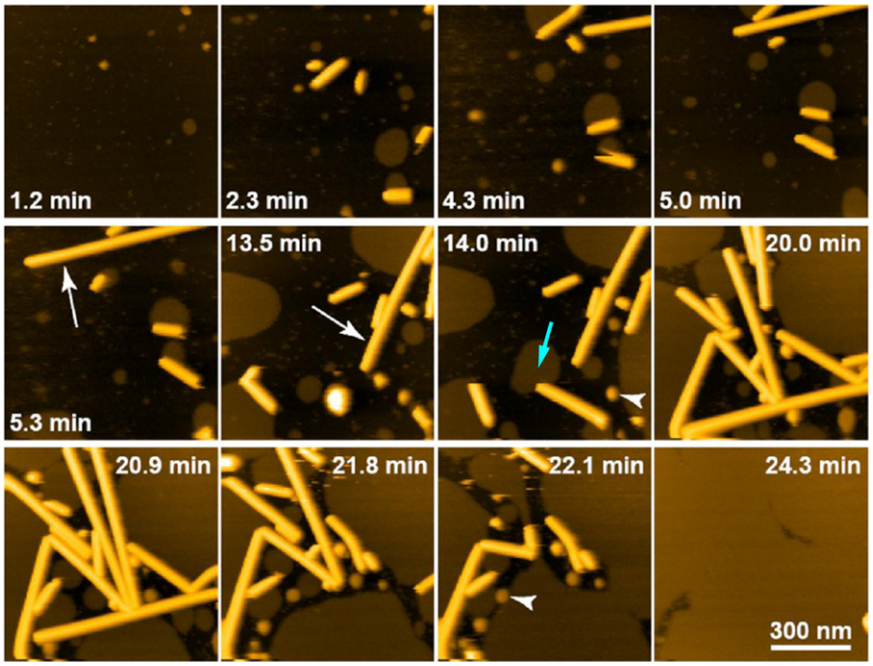

Figure 6. High-speed AFM images showing the process of SLB formation. Lipid membranes were made of a ternary mixture made of DOPC/DOPS/biotin-cap-DPPE in buffer (10 mM HEPES, 150 mM NaCl, 2 mM $CaCl_2$, pH 7.4). The liposome suspension (0.5 mg ml^{-1}) was then directly diluted into the buffer present in the liquid cell equipped in the high-speed AFM instrument and the bilayer formation was imaged at 1.03 fps (scan size 800 × 800 nm^2). SLB was formed from LNT (white arrows, approximately 20 nm in height) and liposomes (arrowheads, 7.5–30 nm in height). *Z* color scale, 25 nm. The light-blue arrow indicates the interaction between a patch of SLB and one end of an LNT.

5.2. Recent studies

As listed in table 1, several targets and subjects have been fully studied in the most recent 3 years. Here, these studies are classified as (1) 2D crystal systems, (2) isolated proteins, (3) protein self-assembly processes, (4) DNA-binding proteins and synthetic DNA devices, (6) manipulation and imaging, and (7) non-biological studies. Below, at least one topic is highlighted for each class of study, except for non-biological studies.

5.2.1. 2D crystal systems. 2D crystal systems studied thus far are mica surface-supported planar lipid bilayers [98], detergent micelles (movie S3 available at stacks.iop.org/Nano/23/062001/mmedia) [112], native membrane proteins (bacteriorhodopsin (bR) [81, 92, 113] and ATP-synthase c-rings in a native lipid membrane [101]), and 2D crystals of streptavidin [76, 82] and annexin A–V [93] formed on mica-supported planar lipid bilayers.

5.2.1.1. Planar lipid bilayers. Small lipid vesicles (single-lamellar vesicles), which are prepared by sonication of large multi-lamellar vesicles, attach to a negatively charged mica surface by electrostatic interaction and then rupture. Upon rupture, small patches of supported lipid bilayers (SLBs) are formed. These patches are fused into larger SLBs and eventually the entire mica surface is completely covered by the bilayers. This entire process was revealed for the first time using high-speed AFM.

The SLB formation process was recorded in depth in the collaboration between my group and Le Grimellec's group (movie S4 available at stacks.iop.org/Nano/23/062001/mmedia) [98]. The lipid composition of small vesicles used was DOPC:DOPS:biotin-cap-DPPE = 6:2:2 (w/w) suspended in 10 mM HEPES–NaOH (pH 7.4), 150 mM NaCl and 2 mM $CaCl_2$ (DOPC: dioleoylphosphatidylcholine; DOPS: dioleoylphosphatidylserine; biotin-cap-DPPE: 1,2-dipalmitoyl-*sn*-glycero-3-phosphoethanolamine-*N*-(capbiotinyl)). The imaging was carried out over 25 min at 1.03 fps for a scan area of 800 nm × 800 nm. An unexpected phenomenon observed was the formation of lipid nanotubes (LNTs) of ∼20 nm diameter (figure 6). Short LNTs had already been formed in the vesicle sample before the deposition onto a mica surface as they appeared together with small globular vesicles in the AFM images immediately after the deposition. Unlike the globular vesicles, the short LNTs did not rupture on the mica surface and grew longer by two mechanisms; (1) addition of free lipids to the free ends and (2) the end-to-end fusion of LNTs. The LNTs also interacted with the edge regions of SLBs either at their longitudinal sides or at one of the free ends. In the latter case, the interacting SLBs were getting smaller. With the lapse of time, the length and density of LNTs increased and the size of SLBs also increased. As a result, long LNTs were jammed into narrow spaces between large SLBs, thus pushing each other and eventually rupturing. After the rupture, the size of SLBs immediately increased to cover large areas of the bare mica surface.

As demonstrated by this observation, various dynamic events appear simultaneously in a molecular movie (movie S4 available at stacks.iop.org/Nano/23/062001/mmedia), which is one of the powerful features of high-speed AFM. The high

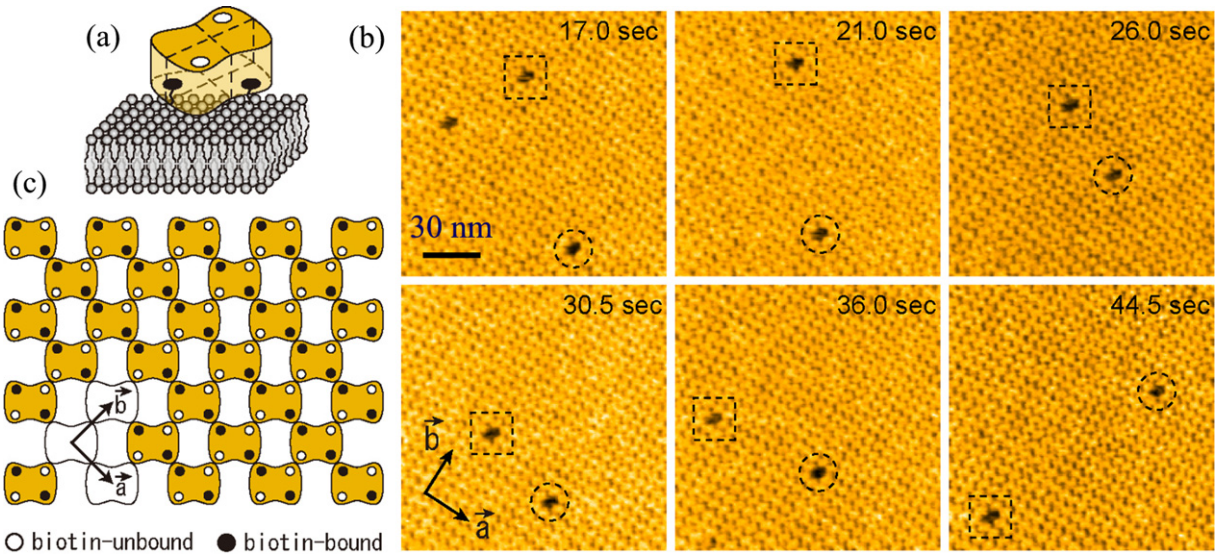

Figure 7. Defect diffusion in streptavidin 2D crystal. (a) Schematic of a streptavidin molecule on biotinylated lipid bilayer. Two biotin binding sites occupied by biotin are indicated by the closed circles. The open circles indicate biotin binding sites facing the aqueous solution and are biotin-free. (b) High-speed AFM images of streptavidin 2D crystal with *C*222 lattice and monovacancy defects therein. The monovacancy defects are enclosed by dashed squares and circles. The directions of the lattice vectors of the crystal are also indicated. Successive images were obtained at an imaging rate of 2 fps with a scan area of 150 × 150 nm^2 and the number of pixels was 200 × 200. (c) Schematic of streptavidin arrays in *C*222 crystal. Unit lattice vectors are indicated. The *a* axis includes rows of contiguous biotin-bound subunits, while the *b*-axis includes rows of contiguous biotin-unbound subunits.

stability of LNTs can be accounted for by the smaller surface curvature (and hence smaller surface tension), compared with that of small globular liposomes. In the sideways surfaces of the edge regions of SLBs and the ends of LNTs, the polar head groups rather than alkyl chains are exposed. The arrangements of lipid molecules at these surfaces are energetically unfavorable compared with those in the flat surface area of SLBs and the longitudinal surfaces of LNTs. Therefore, to reduce the fraction of these unfavorable surfaces, SLBs and LNTs grow by incorporating free lipids and by fusing with the respective kind of partners. As mentioned above, when one of the ends of an LNT was brought into contact with a sideways edge of an SLB patch, the size of the patch became smaller with time, indicating that lipids are transferred from the SLB to the LNT, although the concomitant growth of the LNT was not apparent. The SLBs are thin (a few nanometers) while the LNTs are ∼20 nm in diameter, so that the arrangements of lipids facing at the sideways edges of SLBs are energetically unfavorable, compared with those of lipids at the ends of LNTs. This energetic difference would account for the lipid transfer. The mechanism underlying LNT formation and the molecular packing in an LNT are still elusive. It would be likely that the LNTs have a double-layered or monolayer-stacked structure with a hollow in the center, as has been revealed for different LNTs [126, 127]. LNTs naturally occur in life and synthetic LNTs are expected to have various applications including encapsulation of drugs. A study similar to the above was recently carried out using a cationic surfactant, aiming at an eventual goal of elucidating the process of cleaning by detergents at the nanometer scale [112].

As will be described later, SLB surfaces are useful for anchoring a specific protein species without non-specific adsorption of other species. This selective anchoring facilitates AFM imaging of dynamic interaction events of samples containing multiple protein components [93].

5.2.1.2. 2D crystals of proteins on SLBs. 2D crystals of proteins formed on SLBs have been widely studied for various purposes; e.g. structural determination of proteins by electron diffraction [128], understanding of crystal formation [129] and practical use of the surfaces as substrates. For the efficient formation of 2D protein crystals on SLB surfaces, the SLB should be highly fluidic. Lipids with unsaturated alkyl chains such as DOPC are often used for preparing highly fluidic SLBs. To attach a protein to an SLB surface, lipids with functional groups or electrically charged lipids are included in the SLB [93]. Here, atopic of dynamics involved in 2D protein crystals is described.

The topic is diffusion of point vacancy defects in the orthorhombic *C*222 crystal of streptavidin formed on biotin-containing SLBs (movie S5 available at stacks.iop.org/Nano/23/062001/mmedia) [76]. Note that the 2D crystal has *P*2 symmetry [82] but here the notation *C*222 for the symmetry group follows a previous report [130]. Streptavidin is a homotetrameric protein with dihedral *D*2 symmetry and each subunit specifically binds to one biotin. Streptavidin is easily crystallized in 2D forms on biotinylated SLBs. On the biotinylated SLBs, two of the four biotin binding sites face the lipid layers and are occupied by biotin, while the other two are exposed to the aqueous environment and therefore are biotin-free (figure 7(a)). The lipid composition used was DOPC, DOPS and biotin-cap-DOPE (7:2:1 w/w). The *C*222 crystal of streptavidin with lattice constants $a = 5.9 \pm 0.1$ nm, $b = 5.9 \pm 0.3$ nm and $\gamma = 90°$ was prepared using a buffer solution containing 10 mM HEPES–NaOH, 150 mM NaCl and 2 mM $CaCl_2$ (pH 7.4). Monovacancy defects in the

streptavidin 2D crystals were produced by increasing the tapping force exerted from the oscillating tip to the sample. The imaging was carried out at 2 fps over 150×150 nm^2 scan areas.

As shown in figure 7(b), monovacancy defects were mobile, with an anisotropic feature with respect to the two axes of the crystalline lattice; larger mobility along the *b* axis than the *a* axis. The *a* axis includes rows of contiguous biotin-bound subunits, whereas the *b* axis includes rows of contiguous biotin-bound subunits. The linear relationship between the mean-square displacements and time intervals gave the diffusion rate constants of $D_a = 20.5$ nm^2 s^{-1} for the *a*-axis component of diffusion and $D_b = 48.8$ nm^2 s^{-1} for the *b*-axis component of diffusion. This anisotropy in the mobility ($D_b > D_a$) arises from a free energy difference between the biotin-bound subunit–subunit interaction and biotin–unbound subunit–subunit interaction. When a streptavidin molecule adjacent to a monovacancy defect moves to the defect site along the *a* axis, two intermolecular bonds between biotin–unbound subunits ('u–u bond') and one intermolecular bond between biotin-bound subunits ('b–b bond') are broken. On the other hand, when it moves to the defect site along the *b* axis, one u–u bond and two b–b bonds are broken (see figure 7(c)). Therefore, the difference in the activation energies E_a and E_b for the step movement of a monovacancy defect along the respective *a* and *b* axes simply corresponds to the difference between the free energy changes $G_{\mathrm{u-u}}$ and $G_{\mathrm{b-b}}$ produced by the formation of the respective u–u bond and b–b bond; namely, $E_b - E_a = G_{\mathrm{u-u}} - G_{\mathrm{b-b}}$. Therefore, the observed relationship $D_b > D_a$ indicates $G_{\mathrm{u-u}} < G_{\mathrm{b-b}}$; namely, the u–u bond affinity is higher than that of the b–b bond. The ratio of the two diffusion rate constants (D_b/D_a) can be expressed by $D_b/D_a = \exp[-(E_b - E_a)/(k_{\mathrm{B}}T)]$, where k_{B} is the Boltzmann constant and T is the absolute temperature. Thus, from the observed value of $D_b/D_a \sim 2.4$, the free energy difference $G_{\mathrm{u-u}} - G_{\mathrm{b-b}}$ is estimated to be approximately $-0.88k_{\mathrm{B}}T$ ($T \sim 300$ K), which corresponds to -0.52 kcal mol^{-1}.

The monovacancy defects sometimes fused into a divacancy defect. Through several fusions, larger multivacancy defects were formed. As the size increased, the diffusivity of multivacancy defects increased for both crystal axes, although the diffusivity of divacancy defects was similar to that of monovacancy defects. The higher mobility of larger point defects increases their probability to encounter other point defects to form larger point defects with further higher mobilities. During the crystal growth in the presence of free streptavidin in the bulk solution, this acceleration effect should promote the removal of point defects from the crystalline regions. This would be one of the mechanisms for defect-free crystal formation not only in 2D crystals but also in 3D crystals. This issue should be examined in the future by imaging the crystal growth in the presence of free streptavidin in the bulk solution.

5.2.1.3. Native membrane proteins. Two topics on native membranes proteins, bacteriorhodopsin (bR) and ATP-synthase c-rings, are highlighted here. In the former, light-induced structural changes are described, while in the latter, membrane-mediated protein–protein interaction is described.

bR in response to light. To explore appropriate conditions for capturing AFM images of high spatial resolution and to demonstrate the high spatial resolution power of AFM, the purple membrane, which contains highly packed 2D arrays of photoreceptor bR molecules, has often been used in preference as a sample to image [131]. In fact, faithful high-resolution images capable of distinguishing the individual interhelix loops of bR are obtained [132]. Nevertheless, the physiologically relevant structural changes in bR (i.e. response to light) have never been captured by AFM until recently. bR functions as a light-driven proton pump, transferring protons across the membrane from the cytoplasmic side to the extracellular side [133, 134]. bR is comprised of seven transmembrane α-helices (named A–G) surrounding the retinal chromophore covalently bound to Lys216 via a protonated Schiff base [135, 136]. In the purple membrane, bR assembles into trimers and the trimers are arranged in a hexagonal lattice. Upon absorption of light, photoisomerization from all-*trans* to 13-*cis* conformation of the retinal chromophore takes place. This isomerization induces proton transfer from the Schiff base to Asp85, which triggers a cascade of changes in the bR structure. A series of intermediates designated J, K, L, M, N and O are defined by spectroscopy, and M (M_{410}), which has an absorption peak at 410 nm and the longest lifetime, is only the intermediate containing a deprotonated Schiff base [134]. The light-induced conformational changes in bR in the frozen activated state of the wild type (WT) and bR mutants have been studied by x-ray crystallography and electron microscopy [137–139]. The extent of the changes reported varies, depending on the methods used, but it is generally small (0.1–0.3 nm). The dynamic nature of the conformational changes, however, remained elusive due to the lack of techniques amenable to the high-resolution visualization of dynamic structural changes of proteins. My group, for the first time, succeeded in capturing high-resolution successive images showing dynamic changes of bR in response to light using high-speed AFM [92].

The photocycle of the wild type at neutral pH proceeds very fast (~10 ms). We attempted to visualize the conformational changes at the highest possible imaging rate of ~80 fps by narrowing the imaging area but were unable to detect discernible changes. To slow down the photocycle, we then used the D96N bR mutant that has a longer photocycle (~10 s at pH 7) but still retains a proton pumping ability [140]. Figure 8(a) presents successive images of the D96N mutant at the cytoplasmic surface captured at 1 fps. Upon illumination with green light (532 nm, 0.5 μW), bR drastically changed its structure (compare images at 1 and 2 s) and returned to the unphotolysed state in a few seconds after light-off (movie S6 available at stacks.iop.org/Nano/23/062001/mmedia). This structural change was reproducible in repeated dark–illumination cycles. Note that this structural change is specifically induced by green light, not by blue

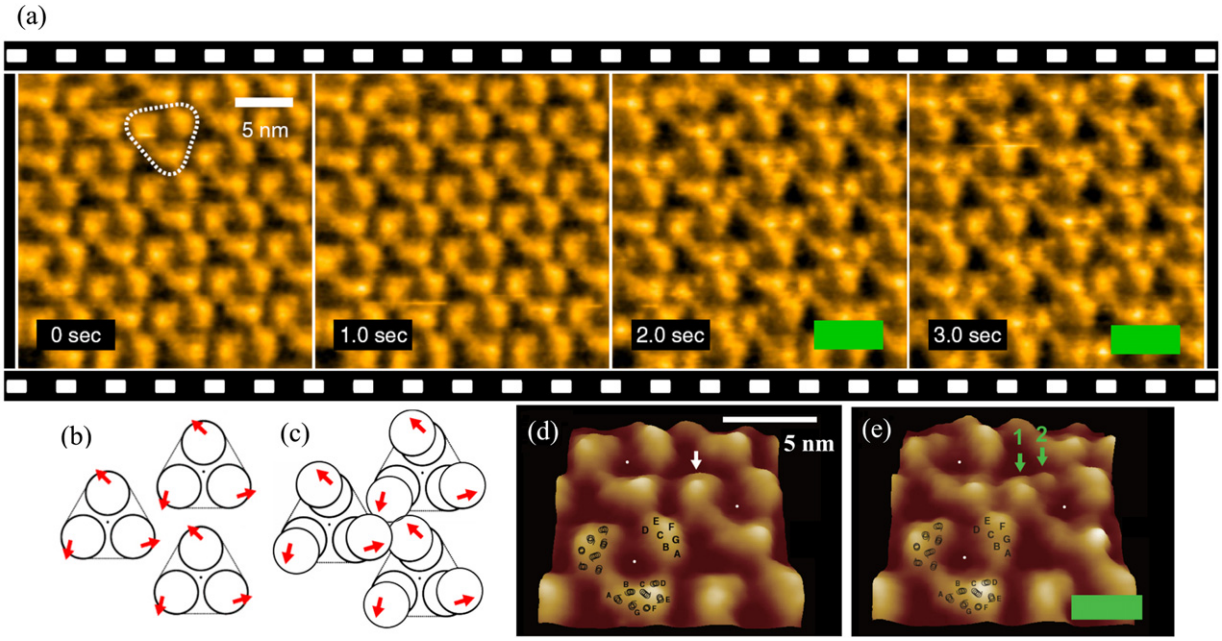

Figure 8. Structural change in bR induced by light absorption. (a) Successive high-speed AFM images of the cytoplasmic surface of D96N bR under dark or illuminated conditions. Frame rate, 1 fps; pixel size, 200 pixels × 200 pixels. A bR trimer is highlighted by the white triangle. The green bars indicate illumination by 532 nm green light of 0.5 μW. (b) Schematic of arrangement of bR molecules and bR trimers under dark. The arrows indicate the directions in which respective bR molecules displace upon light illumination. (c) Schematic of arrangement of bR molecules and bR trimers under illumination. The three bR molecules in a trefoil form a transient assembly. The arrows indicate the directions in which respective bR molecules displaced upon light illumination. (d), (e) Surface maps of the magnified images in the dark (d) and under illumination (e). The position of each trimer center is denoted by the white dots. A monomer in the dark is indicated by a single white arrow. Under illumination, the topography of the monomer splits into major and minor protrusions, as indicated by green arrows 1 and 2, respectively. The positions of seven transmembrane α helices A–G are schematically indicated on the left bottom trimer images.

or red light. This fact clearly indicates that the observed structural change is not an artifact but intrinsic to the nature of bR because bR in the ground state effectively absorbs green light. All the activated bR monomers moved outwards from the centers of respective trimers and rotated counterclockwise around the centers of respective trimers, as illustrated by arrows in figure 8(b). This movement was quantified by calculating the center of mass of each bR monomer. The average displacement was 0.7–0.8 nm and the average rotation angle was 7°–8°. However, the overall position of each bR molecule does not change because of indiscernible alterations at the extracellular surface. The photoactivated state observed by high-speed AFM could be attributed to the spectroscopically identified M intermediate because the lifetimes of other spectroscopic intermediates occurring prior to M are very short. However, it is uncertain whether the photoactivated state detected by AFM also contains the N intermediate that follows M. This issue was solved by another study as mentioned later [113].

Figures 8(d) and (e) respectively show magnified AFM images obtained before and during illumination which are superimposed on the atomic model of the α-helical cytoplasmic ends in the unphotolysed state (A–G) [136]. The protruding parts around helices E and F displace outwards from the trimer center under illumination. Since a previous static AFM imaging study of bR has assigned the prominent protrusion in the AFM topographs of bR to the cytoplasmic E–F loop [132], the protrusion movement visualized here is ascribed to the displacement of the E–F loop. As a result of E–F loop displacement, the protrusion is divided into two sections (green arrows 1 and 2 in figure 8(e)), and the minor protrusion (green arrow 2) likely corresponds to the position around helices A and B. Previous x-ray crystallography and electron microscopy studies could not detect the displacement of loop regions because of their thin and disordered structures. This is the reason why these previous studies only detected a small change (0.1–0.3 nm).

As a result of the outward displacement of the E–F loop, nearest-neighbor bR monomers, each belonging to a different adjacent trimer, transiently assemble, as illustrated in figure 8(c). Here, we use a new designation, ‘trefoil’, for the triad of nearest-neighbor monomers belonging to different trimers to distinguish it from the original trimer. Notably, this transient assembly in a trefoil alters the decay kinetics of the activated state. Figure 9(a) shows the time course of the displacement of the mass centers for six bR monomers belonging to two different trefoils observed at different light intensities (M_n1–M_n3; n indicates different trefoils) (see movie S7 available at stacks.iop.org/Nano/23/062001/mmedia). Under weak illumination, it is mainly the case that only one monomer in each trefoil is activated (M_13 and M_22 in the left panel of figure 9(a)). When only one monomer is activated in a trefoil, it decays with a time constant of 7.3 ± 0.58 s (the top panel of figure 9(b)). In

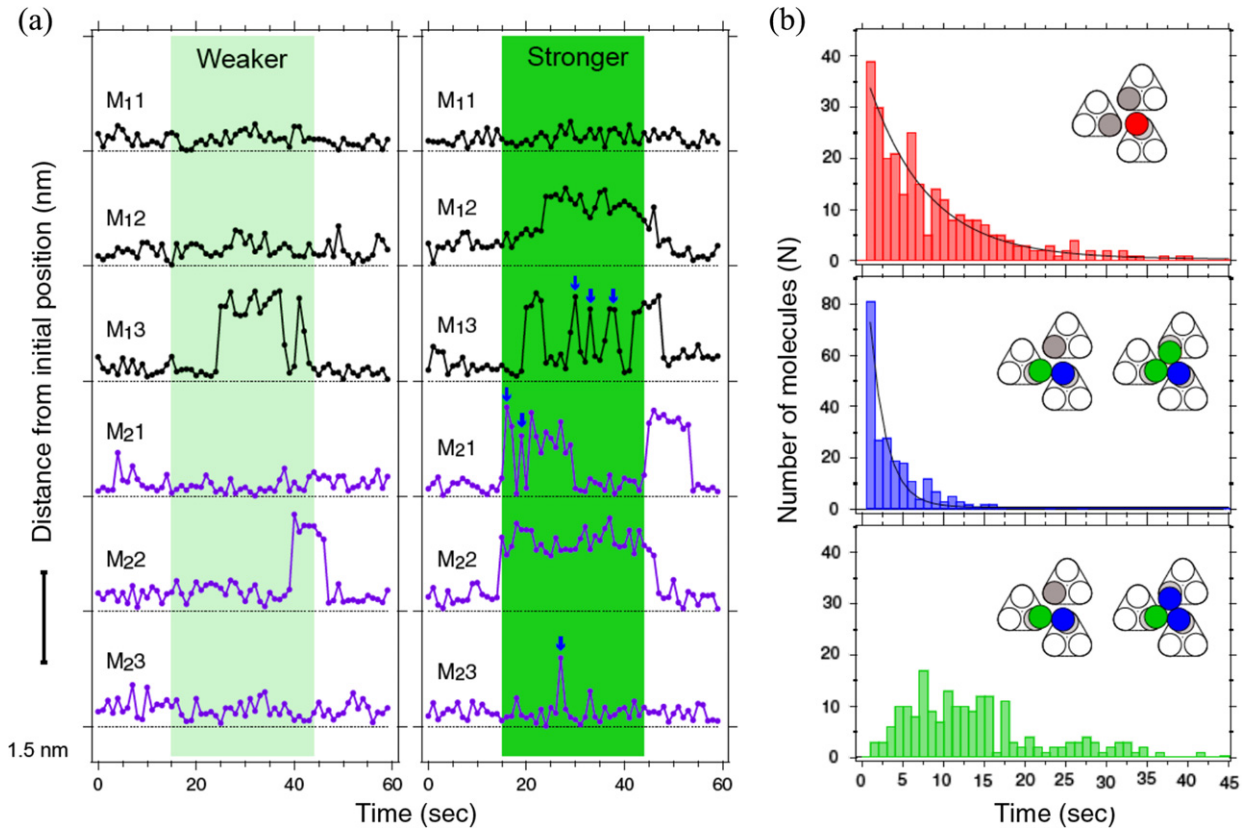

Figure 9. Cooperative effects on the decay kinetics in D96N bR. (a) Displacement of mass center positions as a function of time measured for six bR monomers forming two different trefoils (M_n1–M_n3; n indicates different trefoils) under different light intensities. The green regions correspond to the illumination, and their shade level indicates the relative light intensity (0.007 and 0.5 μW). The blue arrows indicate the conformational changes of the monomers (M_13, M_21 and M_23) that are activated subsequent to the activation of other monomers in the respective trefoils. (b) The top figure shows the decay of activated bR monomers (as depicted by the red circle) while the other monomers (the gray circles) within the respective trefoils are not in the activated state. The exponential decay constant is 7.3 s. On the other hand, when one or two nearest-neighbor molecules (as depicted by green circles in the middle figure) in a trefoil are already activated, the bR monomer activated latest (as depicted by the blue circles in the middle figure) decays faster. The exponential time constant is shortened to 2.0 s. In contrast, the early activated molecules within a trefoil (as depicted by green circles in the bottom figure) show a non-exponential broad distribution of decay time with an average of 13.3 s.

contrast, under stronger illumination, two or three monomers within a trefoil tend to be activated together. Interestingly, the decay of each monomer markedly depends on the order of its activation. The monomer that is activated latest among the activated monomers in the trefoil (blue arrows in the right panel of figure 3(a)) decays with a shorter time constant of 2.0 ± 0.16 s (the middle panel of figure 9(b)). On the other hand, the decay kinetics of the early activated monomers (M_12 and M_22 in the right panel of figure 9(a)) does not follow a single exponential (the bottom panel of figure 9(b)) and the averaged decay time lengthens to $\sim$13 s. This observation indicates that the early activated monomers do not return to the ground state as long as the adjacent monomers within the trefoil are in the active state. Thus, bR–bR interaction within the trefoil (not within the trimer) under illumination engenders both positive and negative cooperative effects in the decay kinetics as the initial bacteriorhodopsin recovers. As a consequence, the turnover rate of the photocycle is maintained constant, on average, irrespective of the light intensity.

This study was followed by experiments where bR was alternately illuminated with green and blue light (movies S8 and S9 available at stacks.iop.org/Nano/23/062001/mmedia) [113]. M_{410} having an absorption peak at 410 nm effectively absorbs blue light. It is known that, after M_{410} is formed upon green illumination, it can be driven back to the ground state (bR_{570}) by blue light [141]. High-speed AFM imaging under alternate illumination revealed that the photoactivated conformation of bR is also driven back to the unphotolyzed conformation without time delay. Thus, conformation of bR is tightly coupled to the conformation of retinal. Next, it was examined whether the activated state of bR observed by AFM contains not only M_{410} but also other intermediates that are spectroscopically different from M_{410}. To address this issue, the photocycle was initiated by brief green light illumination and then blue light was briefly applied with different delay times. Before the blue light is turned on, the fraction of activated molecules is gradually decreasing in the normal course of the photocycle, but it is abruptly decreased nearly to zero after the brief blue light illumination. This abrupt decrease was independent of the time interval between the brief two-color illumination. Thus,

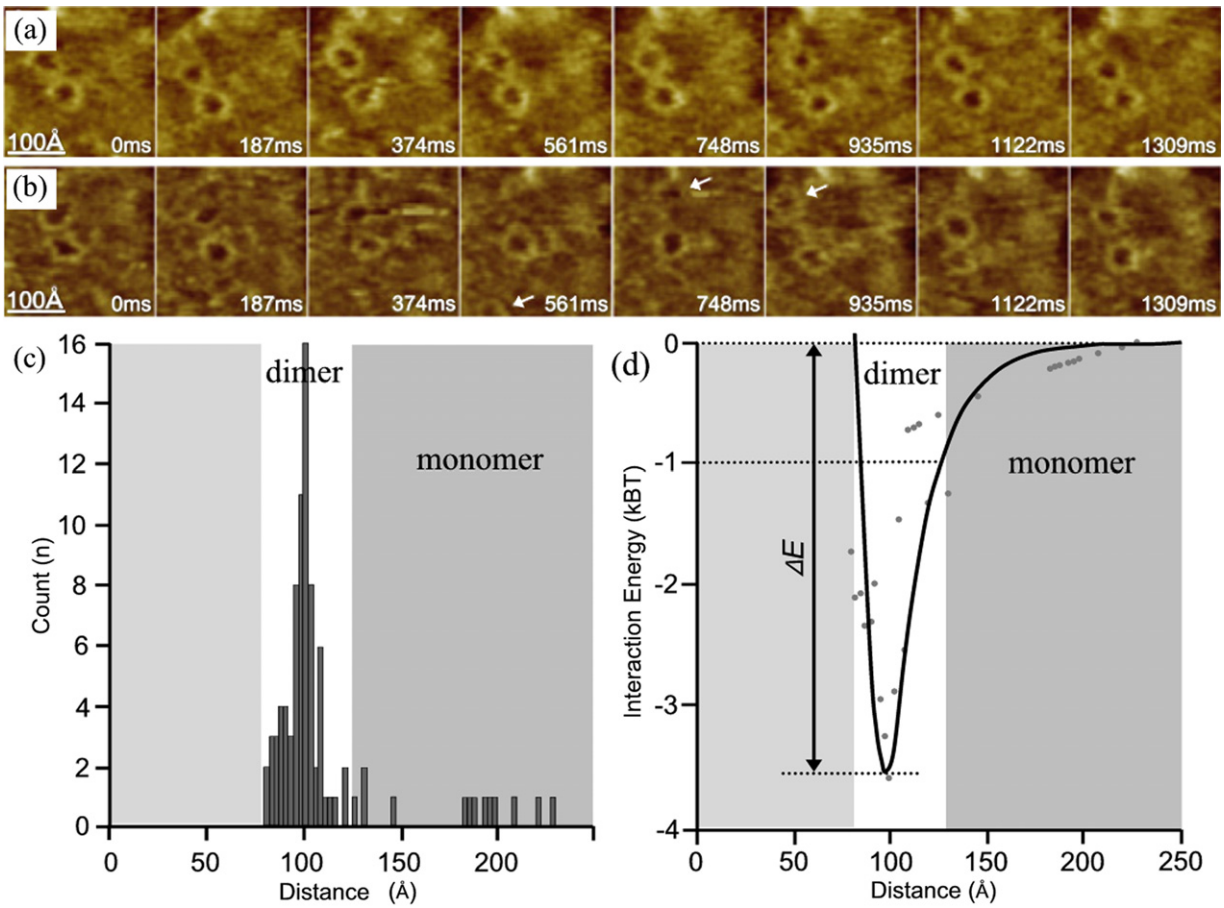

Figure 10. Membrane-mediated interaction between c-rings. (a) Successive high-speed AFM images of c-rings in a dimer. Two c-rings are in a dimer over a time span of 1309 ms. (b) Successive high-speed AFM images of c-ring dimer that dissociates and reforms. One c-ring is intermediately monomeric for ∼400 ms (white arrows in frames: 561, 748 and 935 ms) and subsequently reforms a dimer that resembles the initial assembly. (c) Histogram of the center-to-center distance of c-rings. (d) Membrane-mediated two-protein interaction energy landscape. Reprinted with permission from Elsevier.

it was concluded that the conformation of bR in the activated state observed by AFM solely corresponds to the M_{410}.

The above AFM observations of bR, particularly the bR–bR interaction in the trefoil, concretely exemplified that minute and elaborate functional mechanisms of proteins inaccessible by other techniques can be uncovered by direct visualization of proteins in action at high spatiotemporal resolution.

Membrane-mediated protein–protein interaction. Membrane proteins interact with the surrounding lipid molecules. This interaction affects the structure, function and assembly of the proteins. 'Hydrophobic mismatch' refers to the difference between the hydrophobic thickness of the lipid bilayer and the length of the hydrophobic region of the membrane-embedded proteins [142]. This hydrophobic mismatch at the protein–lipid interface alters the thickness and curvature of the membrane to alleviate the mismatch. When two-protein molecules are in close vicinity, they feel each other through their perturbed membrane fields and then associate with each other to further reduce the energy cost imposed by the hydrophobic mismatch [143].

Scheuring's group studied this membrane-mediated protein–protein interaction by high-speed AFM imaging of the edge regions of the native purple membrane [101]. Many bR trimers diffuse in the fluidic edge regions and a small number of ATP-synthase c-rings also diffuse there [144]. The dynamic association and dissociation between diffusing bR trimers and the crystalline edges were previously imaged (movie S10 available at stacks.iop.org/Nano/23/062001/mmedia) and analyzed by my group and the association energy between two bR molecules was estimated to be $-1.5k_BT$ ($T = 300$ K) per single bond [81]. C-rings with 6.5 nm diameter were observed to assemble into dimers with dynamic association distances ranging from 8–12 nm (figure 10(a)). The dimers rarely dissociated to monomers but were reformed after several hundreds of milliseconds (figure 10(b)). The probability distribution of the center-to-center distance of c-ring dimer $p(d)$ was obtained from the AFM movie[2] (figure 10(c)) and analyzed by the Boltzmann law $p(d) = p_\infty \exp[-U(d)/k_BT]$, where $U(d)$ is the interaction energy and k_BT is the

[2] Available from www.cell.com/biophysj/supplemental/S0006-3495(10)00900-8.

thermal energy. The energy minimum of $-3.5k_BT$ occurred at a center-to-center distance $d = 10.3$ nm (figure 10(d)). This long-range attraction is likely to be caused by the hydrophobic mismatch. In fact, the hydrophobic thickness of phosphatidyl glycerophosphate with a C17 acyl chain, a lipid predominantly existing in the membrane, is ∼2.8 nm, whereas the hydrophobic thickness of the c-rings is about 1 nm larger than the hydrophobic thickness of the lipid bilayer (∼5.6 nm). This presumption was further supported by the measurement of ∼1 nm elevated plateau of the lipid region between the c-rings.

5.2.2. Isolated proteins. Isolated proteins recently imaged by high-speed AFM are facilitates chromatin transcription (FACT) protein [77], cellulase hydrolyzing cellulose fibers [83, 115], ATP-gated $P2X_4$ receptor/channel [90], myosin V walking along actin filaments [91], acid-sensing ion channel 1a under acidification [109] and $\alpha_3\beta_3$ subcomplex of F_1-ATPase (movie S11 available at stacks.iop.org/Nano/23/062001/mmedia) [114]. Some of these studies are highlighted here.

5.2.2.1. Intrinsically disordered FACT protein. There are many proteins or large protein domains that lack a well-defined ordered structure under functional conditions [146, 147]. These new class of proteins are called intrinsically disordered proteins (IDPs). IDPs take a structural ensemble consisting of a large number of random conformers. Upon binding to a target molecule, the disordered structure is often converted to a defined ordered structure. In NMR, the local structure of IDPs can be determined but the overall random structure cannot be provided. Electron microscopy cannot visualize the thin and random structures. Except for computational predictions, there was no way to identify the overall random structure of IDPs.

High-speed AFM has recently demonstrated its ability to visualize the thin and random structures of IDPs, using FACT protein as a test sample [77]. Displacement of histone H2A/H2B dimers from nucleosomes by FACT protein facilitates RNA polymerase II transcription [147] and chromatin remodeling [148]. FACT is a heterodimer consisting of structure-specific recognition protein-1 (SSRP1) and SPT16. Figure 11(a) shows AFM images of a FACT oligomer with four ID regions that are extended from the main body of the oligomer and undulating (movie S12 available at stacks.iop.org/Nano/23/062001/mmedia). The monomer of FACT protein showed two ID regions with different lengths (contour length: 17.5 and 27.5 nm on average). These ID regions were identified by preparing mutants M1 and M2. In M1, the predicted ID regions and the HMG-box domain of SSRP1 were deleted, while in M2 the predicted ID region of SPT16 was deleted. The longer ID region belongs to SSRP1 and the shorter one belongs to SPT16.

Interestingly, both ID regions showed a similar macroscopic flexibility (or stiffness). The stiffness of a polymer chain is described by the persistence length p of the chain, that is, the length over which the average correlation in the

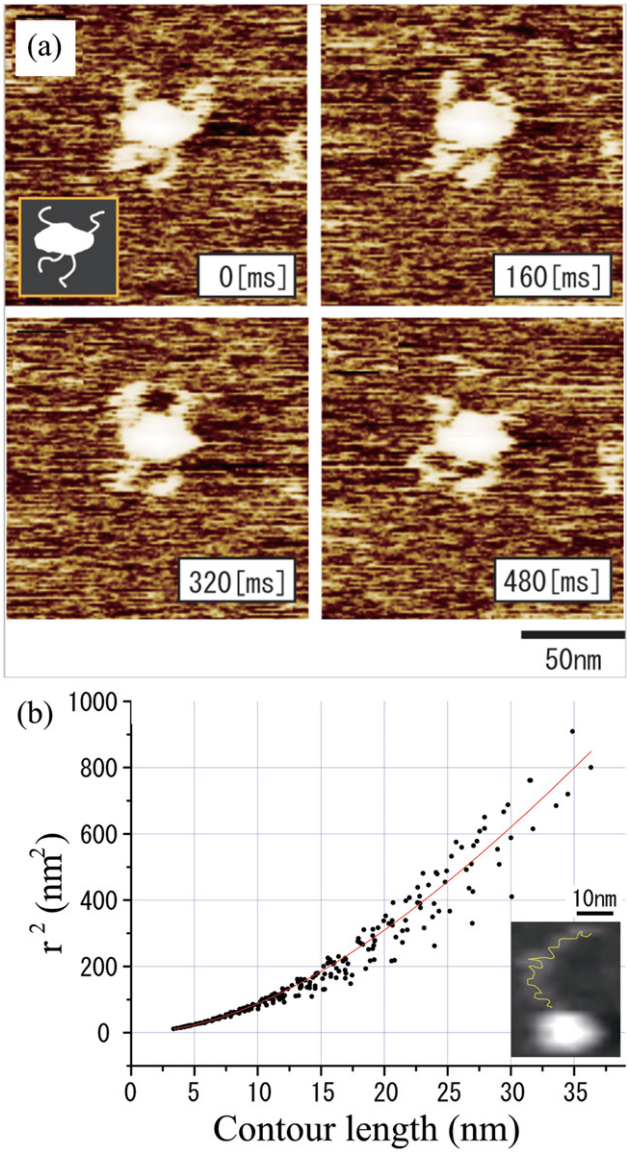

Figure 11. ID regions of FACT protein. (a) Successive high-speed AFM images of oligomerized FACT protein. A lumpy shape and four tail-like structures can be seen (see inset schematic). The position of the tail-like structures fluctuates markedly over time. The images were processed by using brightness-equalizing software. Imaging rate, 6 fps; scan range, 150 × 150 nm^2. (b) Persistence length analysis of ID region of M2 mutant (ID region of SPT16 subunit is deleted). The square point-to-point distance is plotted as a function of the macroscopic contour length between the corresponding two points. The red line indicates the best-fit curve of equation (1) with $p = 12.1$ nm. The inset image indicates the relationship between the microscopic contour and the macroscopic structure. The microscopic contour is schematically drawn with a thin yellow line.

tangential direction decays by $1/e$. In two dimensions, the mean-square point-to-point distance of the chain is given by

$$\langle r^2(l)\rangle_{2D} = 4pl[1 - (2p/l)(1 - \exp(-l/2p))], \qquad (1)$$

where l is the contour length between two points on the chain [149]. In the AFM images obtained for the tail-like structures of FACT, polypeptide chains are not resolved.

Therefore, the persistence lengths that can be obtained from the images are those for overall (macroscopic) string structures. The analysis of AFM images of the ID regions using equation (1) (figure 11(b)) gave a persistence length of 11–12 nm for both ID regions. Microscopic persistence length L_p can be estimated based on an assumption that the polypeptide chain length is a multiple of the number of amino acids and the likely average distance between adjacent amino acid residues (0.34 nm) and on the relationship $\langle R^2 \rangle = 4L_pL$ (L, polypeptide chain length; R, 2D end-to-end distance). This analysis gave a microscopic persistence length of ∼1.1 nm for both ID regions (slightly shorter with the longer ID region, likely due to the presence of the ordered HMG-box domain).

Microscopic measurements of persistence length have previously been performed by measuring force–extension curves by AFM [150, 151], optical tweezers [152] and magnetic tweezers [153]. The microscopic persistence length of the PEVK region (186 amino acid residues), which is responsible for the elastic property of titin and is thought to form a random coil, is reported to show a wide range of L_p (0.4–2.5 nm, on average approx. 0.93 nm) [151]. On the other hand, for proteins with ordered structures, the reported values for the microscopic persistence length are within a range of 0.36–0.5 nm [150, 154]. Thus, the long microscopic persistence lengths of the ID regions of FACT protein are fingerprints of their very loose structures.

As demonstrated above, high-speed AFM is quite powerful in identifying and characterizing ID regions of proteins. In conventional methods, even only the identification of ID regions is difficult and time-consuming. Moreover, high-speed AFM can detect order–disorder transitions of ID regions (unpublished data) that occur naturally with some free ID regions. In the future, high-speed AFM will visualize the process in which ID regions are folded into ordered structures upon interacting with their target molecules and drugs.

5.2.2.2. Walking myosin V. Motor proteins are highly dynamic. They use chemical energy liberated by ATP hydrolysis to generate unidirectional force and motion. The double-headed myosin V (M5), a member of the myosin super-family, moves processively along an actin filament, towards the plus end of the filament (see the review [155]). Facilitated by the processivity of the molecule [156, 157], numerous single-molecule studies have demonstrated that it moves 'hand-over-hand' with a 36 nm advance [158, 159] for every ATP hydrolysis [160]. 'Hand-over-hand' means that the two heads step alternately, exchanging leading and trailing roles with each step, very much like 'walking'. Nevertheless, the comprehensive descriptions of the walking behavior and the chemomechanical coupling have not been attained until our recent high-speed AFM observation of the molecule [91].

Before describing our observation results, let us summarize established facts which are largely common to all classes of myosins. A myosin head is comprised of a motor domain and a neck domain. The motor domain contains two functional sites; the actin-binding and nucleotide-binding sites which communicate with each other. The ATPase reaction proceeds as

$$\begin{aligned} \text{A–M} + \text{ATP} &\rightarrow \text{A} + \text{M–ATP} \rightarrow \text{A} + \text{M–ADP–Pi} \\ &\rightarrow \text{A–M–ADP–Pi} \rightarrow \text{A–M–ADP} \rightarrow \text{A–M}, \end{aligned}$$

where A and M represent actin and myosin head, respectively. Immediately after binding to ATP, the actin-bound head detaches from actin, and then the bound ATP is quickly hydrolyzed to ADP–Pi. The ADP–Pi bound head has a low affinity, yet a somewhat stronger affinity than the ATP-bound head, for actin. When the ADP–Pi bound head is attached to actin, the bound Pi immediately dissociates from the head, which is followed by the formation of a strongly bound complex of A–M–ADP. A nucleotide-free head also has a strong affinity for actin. These strong affinity complexes are called a 'rigor complex'. Thus, a myosin head has two states with respect to actin binding, i.e. weak and strong bound states. The main role of actin in the ATPase reaction is to accelerate the otherwise very slow Pi and ADP dissociation from a myosin head. The degree of acceleration for ADP dissociation varies depending on the class of myosin. The processivity and non-processivity are determined by whether or not the lifetime of A–M–ADP is predominant over the other states [161]. Double-headed myosins can be proteolyzed to produce two single heads. A single-headed myosin binds to actin with a given angle relative to the actin filament. Except for myosin VI, which uniquely moves towards the minus end of actin [162], the bound single head orients toward the plus end of actin at least in the strong bound states. This orientation towards the plus end of actin is called 'arrowhead orientation'.

To observe M5 molecules walking along actin filaments, the filaments have to be immobilized onto a substrate surface while M5 should be free from the surface. We first used an electrically neutral phospholipid bilayer surface containing biotin–lipid, formed on mica. To this surface, tail-truncated M5 (M5-HMM) were never bound, whereas partially biotinylated actin filaments were immobilized through streptavidin. However, in this condition, M5-HMM mostly walked, standing perpendicular to the surface, and hence its molecular shape (sideways figure as illustrated in figure 12(a)) could not be clearly imaged. To facilitate the weak sideways adsorption of M5-HMM onto the bilayer surface, a positively charged lipid (1,2-dipalmitoyl-3-trimethylammonium-propane (DPTAP), 5%) was included in the bilayer. M5-HMM moving processively with ∼36 nm steps was clearly visualized (figure 12(b), movie S13 available at stacks.iop.org/Nano/23/062001/mmedia). The translocation velocity was similar to that measured by fluorescence microscopy when DPTAP was absent in the lipid bilayer, indicating no effect of the tip–sample interaction on the motor activity. The molecular process occurring during a step, however, could not be resolved since a step completes very fast.

Additional streptavidin molecules placed on the substrate surface as moderate obstacles to the advance allowed the visualization of this process (movie S14 available at stacks.iop.org/Nano/23/062001/mmedia). After the trailing head detaches from actin, the leading head spontaneously rotates from the reverse arrowhead orientation to the arrowhead

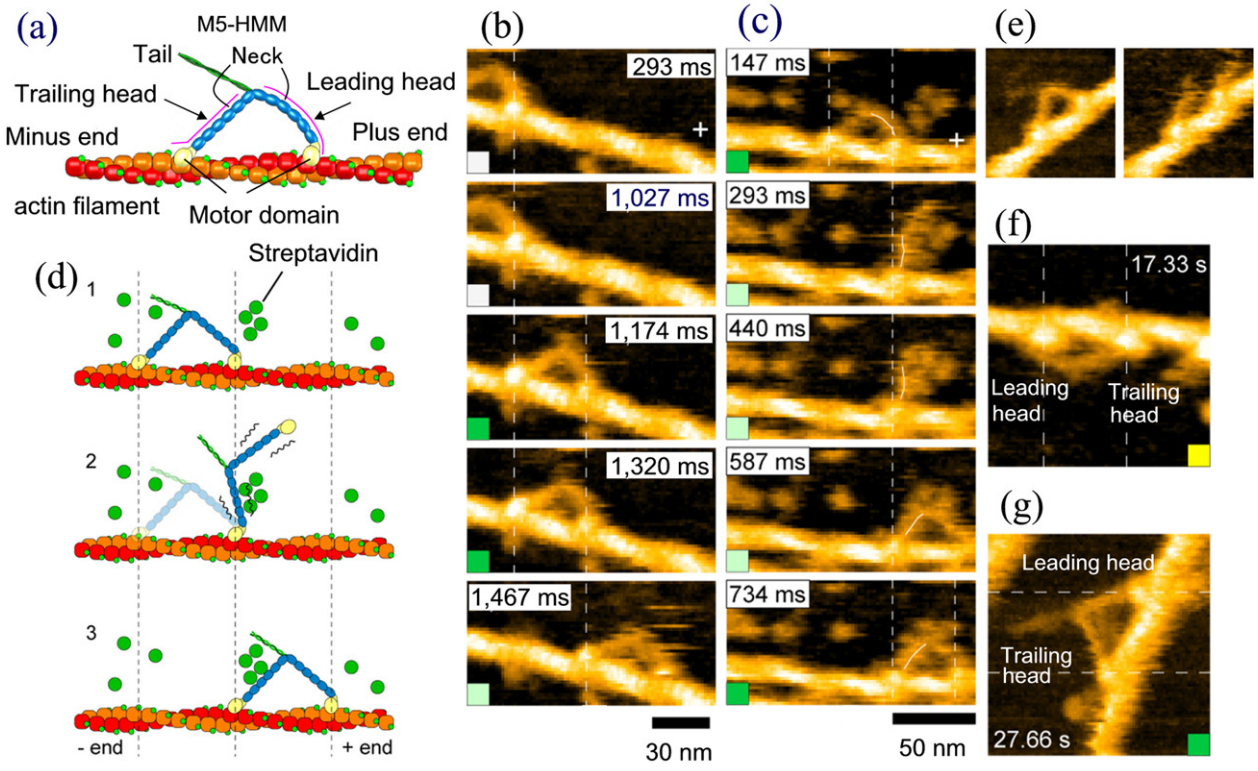

Figure 12. High-speed AFM images of tail-truncated M5 (M5-HMM) interacting with actin filaments. (a) Schematic of two-headed bound M5-HMM. (b) Successive high-speed AFM images showing processive movement of M5-HMM in 1 μM ATP. Frame rate, 7 fps; scan area, 130 × 65 nm^2. (c) Successive high-speed AFM images showing hand-over-hand movement in 1 μM ATP. Frame rate, 7 fps, scan area, 150 × 75 nm^2. The swinging lever is highlighted by a thin white line. (d) Schematic explaining the images in (c). (e) AFM images showing unwinding of the short coiled-coil tail of two-headed bound M5-HMM observed in 50 mM ADP (left panel, before unwinding; right panel, after unwinding). (f) An AFM image of two-headed bound M5-HMM captured under the nucleotide-free condition. The leading head is sharply bent. (g) An AFM image of two-headed bound M5-HMM captured in the presence of 50 mM ADP. The leading head is approximately straight. Vertical or horizontal dashed lines in (b), (c), (f) and (g) show the centers of mass of the motor domains, and a plus sign is used to indicate the plus end of actin.

orientation (figures 12(c) and (d)). This rotation is the swinging lever arm motion itself initially proposed by Huxley for muscle myosin [163], which had never been clearly demonstrated before. The detached trailing head rotates around the advancing neck–neck junction. During the rotation, the head becomes distant from and then gets closer to the actin filament. Finally, it attaches to a forefront actin, completing one step.

The spontaneous rotation of the leading head following the trailing head detachment suggests that intramolecular tension for the advancement has already existed at the leading head of the two-headed bound molecule. This supposition was directly demonstrated by the observation that the short coiled-coil of two-headed bound M5-HMM was sometimes unfolded and then the leading head rotated from the reverse arrowhead orientation to the arrowhead orientation (figure 12(e), movie S15 available at stacks.iop.org/Nano/23/062001/mmedia), very much similar to the swinging lever arm motion during stepping. Thus, we can derive the following conclusions. (1) By nature, both heads most stably bind to actin in the arrowhead orientation but the leading head has to bind in the reverse arrowhead orientation because it is linked to the trailing head at the neck–neck junction and a favorable actin site is already occupied by the trailing head (otherwise the molecule would be forced to twist around the actin filament, paying more energy cost). Thus, intramolecular tension for advancement is generated at the leading head. (2) The detachment of the trailing head removes this constraint imposed to the leading head, thus resulting in the rotation of the leading head. (3) Therefore, this rotation spontaneously occurs without chemical transitions in the ATPase reaction.

It was further observed that the leading head of the two-headed bound molecule was briefly detached from actin and rebound to actin without stepping (‘foot stomp’), and then the molecule stepped forwards (movie S16 available at stacks.iop.org/Nano/23/062001/mmedia). As Pi is quickly released when M5–ADP–Pi is initially bound to actin, the leading head only contains bound ADP before and after foot stomping. Nevertheless, the molecule can step forwards, indicating that intramolecular tension for forward movement is generated without transitioning through Pi release.

Moreover, it was observed that the leading head of the two-headed bound M5-HMM was often sharply bent in the nucleotide-free condition (figure 12(f), movie S17 available at stacks.iop.org/Nano/23/062001/mmedia), while it was mostly

straight in ADP and ATP (figure 12(g)). Therefore, just by looking at the shape of the leading head, we can judge whether or not the leading head contains nucleotides. We imaged two-headed bound M5-HMM in the presence of various concentrations of ADP to estimate the ADP dissociation rate constant at the leading head. The rate came out to be 0.1 s^{-1}. This means that ADP is released from the leading head every 10 s, on average. However, M5-HMM walks many steps for 10 s. Thus, we can conclude that during walking ADP does not dissociate from the leading head (before ADP dissociation, the leading head is switched to the trailing head). ADP dissociation, and the subsequent ATP binding, and the resulting detachment from actin solely occurs at the trailing head. This is the basis underlying the hand-over-hand movement. This mechanism had been suggested from indirect experiments [160, 164–166] but is now clearly and directly demonstrated by the high-speed AFM observation.

Just before foot stomping at the leading head, the head never showed the sharply bent conformation which is unique to the nucleotide-free leading head. This fact reinforces our conclusion that the leading head performing foot stomp carries ADP and thus the brief detachment from actin (i.e. the initial stage of foot stomp process) is not caused by binding of new ATP to the leading head.

As seen above, many dynamic events of M5-HMM appear in the molecular movies, facilitating a quick finding of several facts including those inaccessible with conventional approaches.

5.2.2.3. *Other dynamic processes of isolated proteins.*

Cellulase hydrolyzing cellulose fibers. There are several types of cellulases that hydrolyze cellulose fibers. Cellobiohydrolases (CBHs) are exocellulase that cleaves glycoside linkages of crystalline cellulose I either from the reducing or nonreducing end of cellulose to produce tetrasaccharides or disaccharides [167, 168]. *Trichoderma reesei* (*Tr*) Cel7A composed of a small cellulose-binding domain (CBD) and a larger catalytic domain (CD) is a member of CBHs. Cel7a hydrolyzes cellulose I from its reducing end to produce a β-1,4-glucose dimmer [169]. The two-domain structure is common to glycosidases degrading insoluble carbohydrate substrates. From biochemical kinetics analyses, *Tr*Cel7A is thought to consecutively hydrolyze the crystalline cellulose chain without releasing the chain, and therefore is expected to processively move in one direction during the hydrolysis reaction [170]. Nevertheless, this long-standing issue had never been directly revealed before the high-speed AFM observation recently conducted by Igarashi *et al* [83] and by the collaboration between my group and Igarashi's group [115].

From the biochemically measured hydrolysis rate, *Tr*Cel7A was expected to move on a crystalline cellulose fiber at 1 nm min^{-1}. In marked contrast with this value, *Tr*Cel7A moved at 3.5 nm s^{-1}, ∼200 times faster than expected. This large discrepancy suggests that a large number of molecules cannot smoothly hydrolyze cellulose because of traffic problem [115]. The movement of CBD-truncated *Tr*Cel7A on a crystalline cellulose surface was only observed at >10 times higher concentrations, indicating a low affinity of the CD alone for cellulose. However, it moved at a velocity similar to that of the intact wild-type molecule, indicating that the CBD is not required for the movement. Since *Tr*Cel7A is a small molecule, its molecular conformation was not resolved by the AFM observation, and hence elucidating how the molecule changes its conformation during the processive run remains a challenge.

$P2X_4$ receptor in response to ATP. P2X receptors are ATP-gated membrane cation channels and have seven identified sub-types of subunits ($P2X_1$–$P2X_7$) [171]. Each subunit has two transmembrane domains separated by a large extracellular domain capable of binding to ATP and small intracellular domains at the N and C termini [171]. Channels form as multimers (thought to be mainly trimers) of subunits; homometric or heteromeric channels. All P2X receptors are permeable to small monovalent cations and some have significant Ca^{2+} or anion permeability [172]. P2X receptors are abundantly distributed and involved in diverse physiological processes from synaptic transmission to inflammation and sensation of taste and pain [172]. Crystal structures of the zebrafish $P2X_4$ receptor in the closed-channel state are recently obtained (figures 13(a) and (b)) [173]. The three ATP binding sites are formed at the intersubunits in the trimer, suggesting that ATP binding promotes subunit rearrangement and ion channel opening. The ion channel opening of $P2X_4$ receptor is regulated by the extracellular Ca^{2+} level [174]. In a high concentration of Ca^{2+}, $P2X_4$ receptor opens a small cation-permeable channel pore, whereas in the absence of Ca^{2+}, it forms a large pore allowing permeation of large cationic molecules.

Shinozaki and collaborators imaged ATP-induced conformational changes of $P2X_4$ receptor at 2 fps using two assay systems [90]; isolated (membrane-dissociated) $P2X_4$ attached to polylysine-coated mica and $P2X_4$ reconstructed in a lipid bilayer. In both systems, asymmetric molecules were observed. In the former system, the asymmetry might be due to a leaned orientation of the receptor on the substrate surface. In the latter system it could not be specified. In the absence of ATP, particles observed had a globular shape or a slightly triangular shape, whereas in the presence of ATP under no Ca^{2+}, three subunits were resolved together with a central pore. Interestingly, a pore dilation trimer structure was revealed, whereas in the presence of Ca^{2+}, no pore dilation was observed. Since symmetric molecules were not observed, they used a single-particle correlation averaging method to reconstruct threefold-symmetric images after a given elapse of time. The symmetrized images showed the central pore being dilated with time after the addition of ATP under no Ca^{2+} (figure 13(c)). Since even the membrane-attached receptor shows non-symmetric structures, this non-symmetry may arise from fluctuations of the subunit arrangement in the trimer. In addition, it still remains questionable whether or not the asymmetric trimer structures with pore dilation are an intrinsic nature of this purinergic receptor.

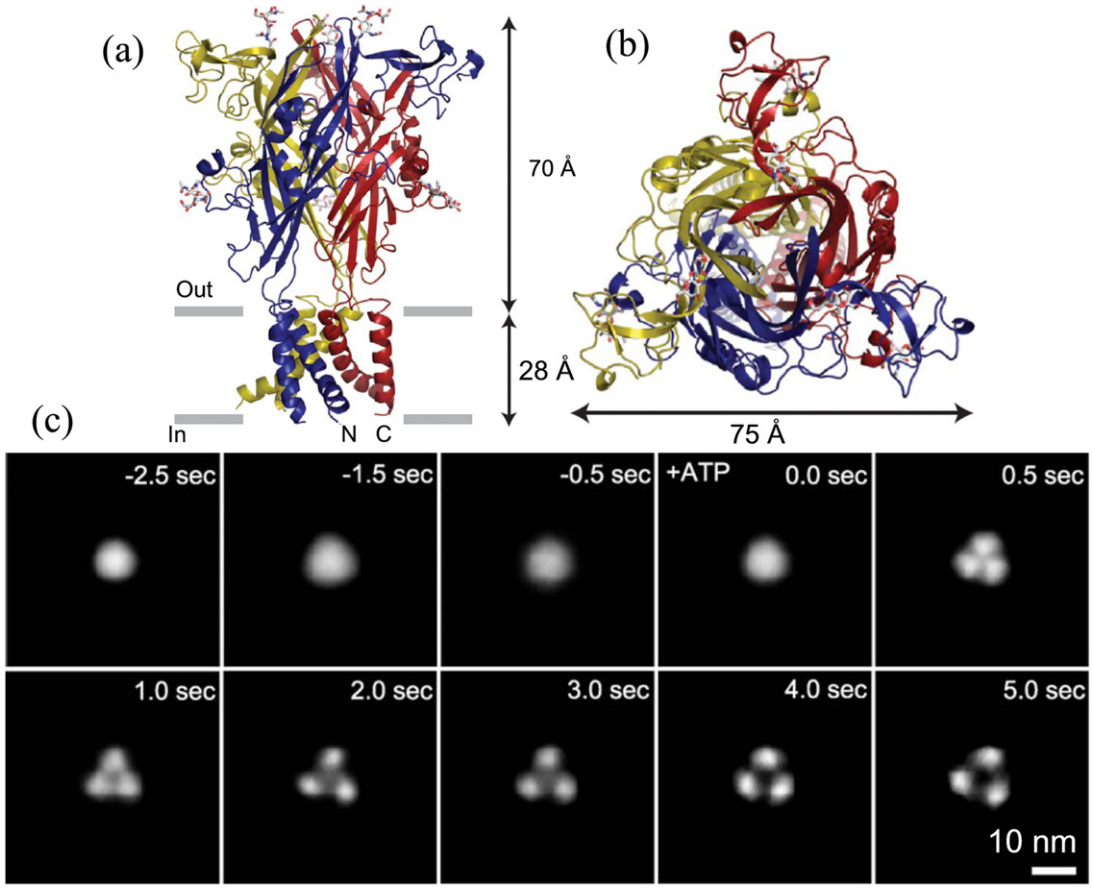

Figure 13. Structure of $P2X_4$ receptor. (a) Atomic structure of N and C termini deletion mutant of homotrimeric $P2X_4$ receptor viewed parallel to the membrane. Each subunit is depicted in a different color. The gray bars suggest the boundaries of the outer (out) and inner (in) leaflets of the membrane bilayer. (b) Atomic structure of N and C termini deletion mutant of homotrimeric $P2X_4$ receptor viewed from the molecular threefold axis (from the extracellular side) (Reprinted with permission from the Nature Publishing Group [173]). (c) Successive AFM images showing ATP-induced structural changes of $P2X_4$ receptor. Before activation, $P2X_4$ receptor was in circular shape and exhibits some fluctuation (−2.5 to ∼0.0 s). Caged ATP (200 μM) was uncaged at 0 s. After uncaging, the structure of $P2X_4$ receptor changed to a trimer structure within 0.5 s. Then, $P2X_4$ receptor exhibited a further structural change and adopted a pore dilation-like conformation. Note that the images are not directly captured ones but are those obtained by averaging images of ten $P2X_4$ receptor particles to reconstruct threefold symmetric images at a given elapse of time.

5.2.3. Protein self-assembly processes. Thus far, this topic other than 2D protein crystal formation has not been studied in depth using high-speed AFM, except for the study of amyloid-like fibril formation by N-terminus-truncated lithosthatine, conducted by the collaboration between the Milhiet group and my group [99]. The polymerization processes of actin and tubulin, which are briefly studied, will be described in section 5.2.5.

Amyloids are insoluble fibrous protein aggregates and their deposition in tissues causes diseases, particularly neurodegenerative diseases [175, 176]. However, the mechanism and dynamics of fibrillization have been elusive. Lithosthatine (also named Reg-1) of 144 amino acids is produced by pancreas acinar cells and secreted into pancreatic juice. It tightly binds calcium carbonate and may act as an inhibitor of calcium carbonate precipitation to prevent clogging of pancreatic duct [177, 178]. In chronic calcifying pancreatitis, the protein forms deposits in the pancreatic duct [179]. Lithosthatine is also expressed in other organs including stomach and brain [180]. Lithosthatine is susceptible to self-proteolysis under specific pH conditions, producing a soluble N-terminal undecapeptide and a C-terminal fragment of 133 amino acids. The cleaved protein (called S1) forms protease-K-resistant fibrils [181] that deposit in the brain of patients with Creutzfeld–Jakob disease [182] and Gertsmann–Straüssler–Scheinker syndrome [183], especially during the very early stages.

The S1 form of lithosthatine was generated by tryptic digestion of the full-length protein. After 15 min incubation, globular structures with 15–28 nm in diameter appeared. They appear to be small assemblies of lithosthatine tetramers with 9 nm in diameter and 2.5 nm in thickness. After 30 min incubation, protofibril formation and its growth to longer protofibrils and thicker fibrils were observed (figure 14). Lengthening of protofibrils takes place at 27–52 nm s^{-1}. Elongation of protofibrils occurs in two ways; (1) addition of lithosthatine oligomers to the ends of protofibrils (white arrows in figure 14) and (2) fusion of a growing protofibril to a pre-existing protofibril (light-blue arrows in figure 14). Interestingly, the end of the pre-existing protofibril to be

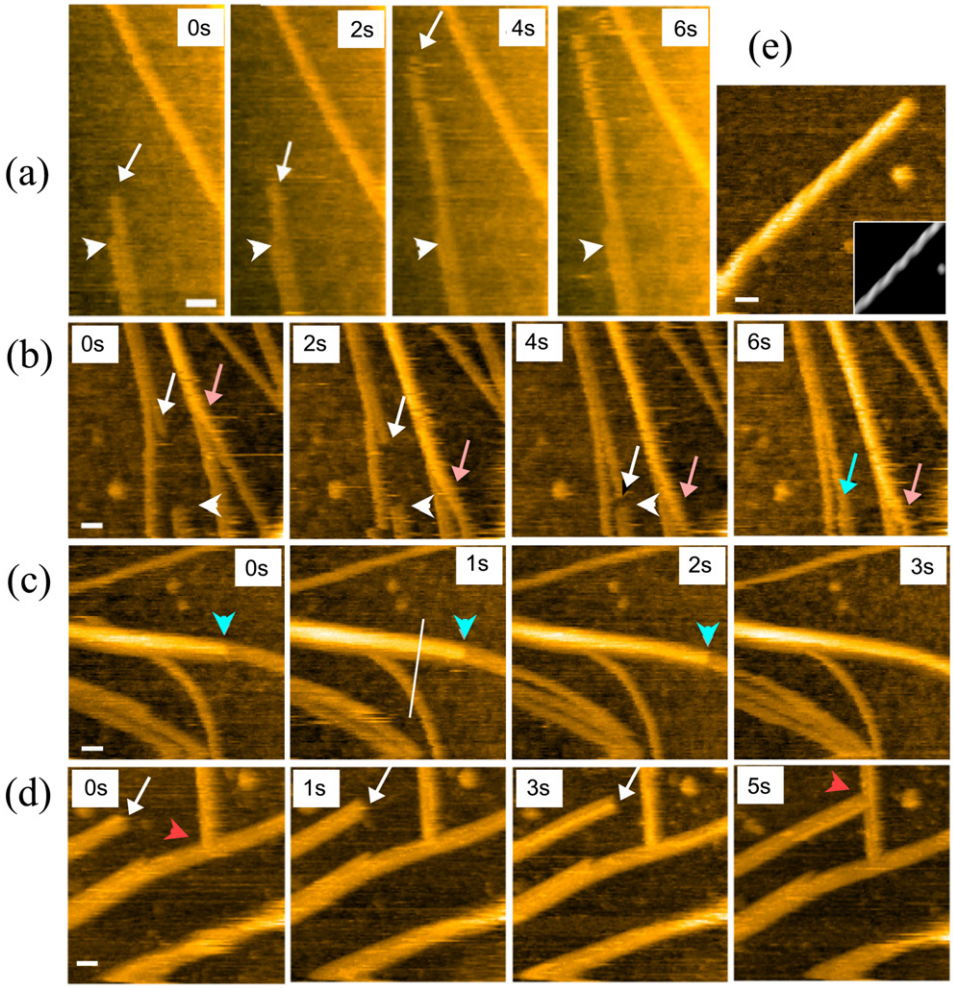

Figure 14. High-speed AFM images showing the time lapse of lithosthatine protofibril elongation and association. Elongation of single protofibrils is shown by white arrows in (a), (b) and (d). Some protofibrils do not grow in length, as indicated by white arrowheads in (a) and (b). Interestingly, the edge of an elongating protofibril can be fused with that of a pre-existing protofibril, forming a continuous structure, as marked with a light-blue arrow in (b). Protofibrils are often laterally associated with another, at least for one part of their length. The complete sideways association between two protofibrils occurs in a zipper-like mechanism (pink arrows). Elongation of a protofibril also occurs, being stacked on a fibril, as indicated with the light-blue arrowheads in (c). The growth of a protofibril or fibril is stopped when the growing end encounters a side edge of a second fibril, forming a false branching point with a certain range of contact angle, as indicated with red arrowheads in (d). Winding of two protofibrils can form helical fibrils (e) (the inset is a filtered image). Scale bars, 30 nm.

fused with the growing protofibril does not change its position (white arrowheads in figure 14(b)), which may suggest a marked difference in the oligomer addition rate at the two ends of a protofibril. Elongation of fibrils appears to occur separately at each constituent protofibril. In fact, a protofibril is elongated on top of laterally associated protofibrils (light-blue arrowheads in figure 14(c)). The lateral association of protofibrils to fibrils takes place in a zipper-like mechanism (pink arrows in figure 14(b)). In the initial stage, two protofibrils make contact with each other in a small region, showing a Y shape. Then, the distance between the separated protofibrils is getting closer to each other by gradual increase of the contact region, and eventually the two protofibrils are completely associated to form a helical fibril similar to other amyloid ß fibrils (figure 14(e)). It is also clear that a branched structure previously observed with lithosthatine fibrils is a false structure. The growth of a protofibril or fibril is stopped when the growing end encounters a side edge of a second fibril, forming a false branching point with a certain range of contact angle (red arrowheads in figure 14(d)). Thus, the dynamic visualization of lithosthatine fibrillization revealed various elementary processes contained in the fibrillization.

5.2.4. DNA-binding proteins and synthetic DNA devices. Regarding DNA–protein interactions, there are a wide range of subjects to be studied by high-speed AFM imaging but only a few studies have thus far been performed; reaction by methyltransferase restriction enzymes [84, 104], unwrapping of DAN–histone complex [108] and reaction by DNA base-excision repair enzyme [103]. Synthetic DNA nanodevices are also interesting targets of dynamic AFM imaging. The specific interactions between complementary base pairs make DNA a useful building material for constructing two- and three-dimensional nanostructures [184]. Various planned

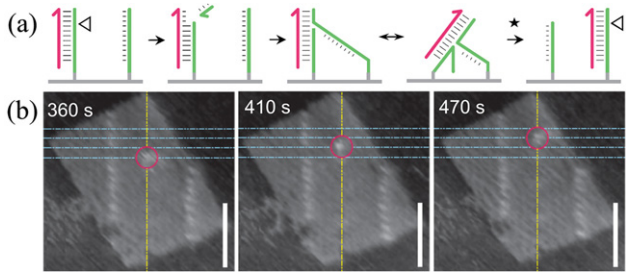

Figure 15. DNA motor movement along the track of DNA stators formed on a DNA origami tile. (a) Motor mechanism: a nicking enzyme (triangles) cuts the stator (green) when the stator is bound to the motor (magenta), revealing a toehold at the 3′ end of the motor that facilitates transfer of the motor to the adjacent intact stator by branch migration. This chain of processes is repeated and thus the motor continuously moves along the track of stators until reaching the track end. (b) Successive AFM images showing discrete steps of a single DNA motor. The highest point on each profile along the yellow line is interpreted as the motor position and marked by the red circle. The motor steps between four stators (blue lines). Imaging rate, 0.1 fps; vertical scale bar, 50 nm. Reprinted with permission from the Nature Publishing Group.

structures can actually be constructed by rationally designing base sequences of DNA. This technique has been used to prepare DNA origamis [89, 107, 117], capsules [110] and nanorobots [118]. Here, a study on dynamic imaging of a nanorobot is taken up.

Dynamic imaging was conducted for a DNA nanorobot in the collaboration between Sugiyama's group and Turberfield's group [118]. Before this study, several types of DNA nanorobots with or without an autonomous motility and processivity have been synthesized including bipedal walkers and rotary gears [185, 186]. However, the motion of these nanorobots has been detected in indirect ways and therefore mechanistic details of their operation have remained elusive.

The nanorobot they constructed consists of an extended track formed on a DNA origami tile (∼70 nm × 100 nm) and a motor DNA. The track consists of a one-dimensional array of single-stranded attachment sites (stators) with the 3′ end at the bottom, separated by ∼6 nm. The motor is a single strand of DNA that is complementary to a stator. A motor–stator duplex contains the recognition site for a restriction enzyme (Nt.BbvCl) that hydrolyzes a specific backbone linkage of the stator. The motor translocation is fueled by the DNA hydrolysis. When the motor DNA hybridizes to a stator strand to form a double strand, the enzyme cuts the stator and removes a short segment from the stator. Therefore, at the 3′ end of the motor a toehold for binding to the adjacent intact stator is revealed. After the actual binding of the toehold, the motor completely dissociates from the nicked stator and completely associates with the neighboring intact stator by branch migration (figure 15(a)). This process is repeated and thus the motor moves processively in one direction along the stator track. The film captured by high-speed AFM at 0.1 fps showed that the motor DNA migrates forwards with discrete steps of ∼7 nm and dwell times of ∼50 s (figure 15(b)) but often moves back and forth between two adjacent stators. This back-and-forth movement suggests incomplete migration of the motor between a cut stator and an adjacent intact stator. The irreversible migration to an adjacent stator appears as transitional shifts of the motor position. These dynamic processes are more directly revealed than previous approaches. However, the spatiotemporal resolution of the movie data was not high enough, so the expected sequential events contained in the motor migration, such as restriction enzyme binding, digestion of a motor-bound stator and intermediate states prior to stepping of the motor, and branch migration, were not well resolved. More detailed molecular events could be visualized if the arrangement of the stators was altered from the vertical to the horizontal orientation and the imaging rate is increased.

5.2.5. Manipulation and imaging. The cantilever tip can also be used to manipulate the sample. Changes in the sample after the manipulation can be traced by imaging using the same tip. The use of high-speed AFM in this way has been attempted in a few studies; formation of vacancy defects in streptavidin 2D crystals and subsequent observation of Brownian motion of the defects (as already described in section 5.2.1.2) [76], breaking actin filaments in the presence of G-actin and subsequent observation of repolymerization processes [82], breaking microtubules in the presence of tubulin and subsequent observation of repolymerization processes (unpublished), and removal of magnetosomes from a substrate surface and subsequent observation of molecules transferred from magnetosomes to the surface [94]. Among these studies, a study on actin polymerization is briefly described below.

Actin filaments have a structural polarity, so that the polymerization kinetics is different at the two ends of the filaments; a higher rate at the barbed end than at the pointed end. Previous fluorescence microscopy studies on the polymerization dynamics with individual actin filaments have suggested that a polymerization unit is not a monomer alone but an average of monomers, oligomers and fragments [187, 188]. However, analysis of precise molecular events occurring at the filament edges was difficult due to the limited spatial resolution.

In the high-speed AFM observation, partially biotinylated actin filaments were attached to a surface of streptavidin 2D crystals formed on biotin–lipid bilayers in the presence of non-biotinylated G-actin in the bulk solution. Instead of finding actin filament ends, they were produced by breaking an actin filament by applying an increased tapping force. This manipulation allows simultaneous visualization of both barbed and pointed ends in a relatively small imaging area. After breaking, elongation was only observed at one of the newly created ends in the observation period and its rate was 0.11 μm min^{-1}, which is comparable to the values obtained previously by fluorescence microscopy. The elongation step size is distributed around two values (3.1 and 5.2 nm), indicating monomer and dimer addition to the barbed end in light of the axially staggered two-stranded structure. Interestingly, a stepwise decrease (3.5 ± 1.4 nm) in the length was occasionally observed, indicating that monomer dissociation is predominant. Moreover, the stepwise decrease

in the length often occurred after monomer addition. The end structure is the same for both cases of monomer and dimer addition. Nevertheless, monomer dissociation more frequently occurred after monomer addition. This suggests that the added monomer possesses ATP while the added dimer possesses ADP.

The approach of manipulation followed by imaging will have a wide variety of applications. As exemplified above, self-assembly processes can be studied by tracing re-assembly processes after breaking an assembled structure. One of the other useful applications is to examine a complicated molecular architecture of a large protein with several domains or a molecular assembly with different subunits. This approach is particularly useful when its structure projected to a 2D plane is known from the electron micrographs but its 3D structure is unknown. Another application is to examine the cooperative interaction between subunits of a protein. For example, ring-shaped AAA proteins, which are often hexamers of identical ATPase subunits, are supposed to show large structural changes during ATP hydrolysis via cooperative interplay between subunits. The cooperative structural changes will be abolished by removing one or two subunits from the ring. This approach was recently utilized to reveal the cooperative interplay between β subunits in the $\alpha_3\beta_3$ subcomplex of F_1-ATPase (a pseudo-sixfold-symmetric ring) [114]. The cooperative structural change in β propagated in the counterclockwise direction during ATP hydrolysis but the occasional subunit dissociation completely stopped the rotary propagation of the conformational state.

5.3. Summary of high-speed AFM imaging studies

As described above, dynamic AFM imaging has already been conducted for a variety of samples. About half of the studies in the last 3 years seem to be aimed at exploring the capability of this new microscopy and groping for effective applications. This situation is quite similar to that in the earlier bio-AFM studies after the advent of AFM in 1986. The dynamic AFM imaging studies carried out thus far can be classified according to the information obtained.

(1) Imaging of dynamic events occurring in the interaction between molecules, in which the observed structure of individual molecules has no importance in the derived conclusion. Typical examples of this class are the studies on membrane-mediated protein–protein interaction [101] and dynamic interaction of isolated bR trimers with the edge of bR 2D crystals [81].

(2) Imaging of dynamic events occurring in the interaction between molecules, in which the structure of individual molecules is not well resolved. Typical examples of this class are the studies on unidirectional translocation of cellulase along cellulose fibers [83, 115] and transportation of synthetic DNA motor along a series of DNA stators [118]. The study on translocation of *Eco*RII restriction enzyme along DNA [74] also belongs to this class.

(3) Imaging of dynamic structural changes of molecules in action. Typical examples in this class are studies on walking myosin V along an actin filament [91], photo-induced structural change in bR [92, 113] and rotationally catalyzing $\alpha_3\beta_3$ subcomplex of F_1-ATPase [114].

Thus, there are two types of dynamics studied by high-speed AFM; 'interaction dynamics' and 'structural dynamics'. In the former type of studies, structural dynamics of individual molecules would have allowed more detailed analysis of the observed interaction dynamics. The lack of structural information at the sub-molecular level arises from three factors. The first factor is the insufficient sharpness of a cantilever tip. The tip apex radius of commercially available small cantilevers is $\sim$15 nm, insufficient for sub-molecular resolution imaging. Small cantilevers with EBD tips are also commercially available but expensive. The apex radius of an EBD tip is often 4–5 nm, still insufficient for resolving sub-molecular structures of small protein molecules, although a $\sim$0.5 nm radius can sometimes be obtained. So, small cantilevers with carbon nanotube tips with an apex radius of $\sim$1 nm are desired, but the procedure is laborious and therefore cannot be used routinely. We need to explore new methods and different materials for fabricating sharp and rigid EBD tips. The second factor is Brownian motion of molecules, particularly in isolated protein molecules. This is a problem intrinsic to AFM imaging of dynamic events because dynamic AFM imaging requires freedom of movement to molecules to some extent. In some cases, the reduction of the Brownian motion can be achieved by devising appropriate substrate surfaces, as has been done for imaging walking myosin V molecules [91]. The third factor is the orientation of the sample relative to the substrate surface. AFM imaging can only be done from the direction perpendicular to the substrate surface. When a molecule stands up on the substrate surface, we cannot see the sideways figure of the molecule. In some cases, a molecule can be placed on a substrate surface in a desired orientation by preparing appropriate substrate surfaces, as has been done for imaging the sideways figures of walking myosin V molecules [91]. It can also be done by introducing a functional group to a specific locus of a molecule and by preparing a substrate surface able to bind to the functional group, as demonstrated in the observation of the sideways figure of GroEL molecules [82] and the C-terminal top surface of the $\alpha_3\beta_3$ subcomplex of F_1-ATPase [114]. Dynamic AFM imaging of biomolecular processes imposes various requirements on 'wet techniques'. This issue is described elsewhere [82, 93].

Various conditions are required for successful dynamic AFM imaging. Nevertheless, once successful, acquired molecular movies are striking. Various dynamic events appear unselectively and simultaneously in a molecular movie, which facilitates quick finding of several facts including those inaccessible with conventional approaches. Thus, the high-speed AFM imaging of functioning biological molecules has the potential of transforming the fields of structural biology and single-molecule biology. In addition, this new microscopy is applicable to the observation of non-biological dynamic phenomena occurring at the solid–liquid

interfaces [96, 97, 112], including electrochemical reactions, corrosions, catalytic reactions and cleaning with detergents. This microscopy will, therefore, facilitate creation of new 'wet nanotechnology'.

6. Future challenges

The current high-speed AFM is powerful in visualizing dynamic events of isolated and purified biological molecules but not applicable to the dynamic observation of the outer surface and the interior of live cells (i.e. *in situ* imaging). Solutions for these challenges and the improvement of the current high-speed AFM are now being developed.

6.1. Small cantilevers

The feedback bandwidth of the current high-speed AFM apparatus exceeds 100 kHz, and consequently an imaging rate of 25 fps is achieved under the condition of 200 nm scan size and 100 scan lines. Can we go beyond? The main device limiting the speed is the small cantilevers. Generally, to improve the resonant frequency, one must compromise the stiffness and vice versa. The most advanced small cantilevers developed by Olympus are deemed to have almost achieved the ultimate goal of balancing these two mechanical quantities. Considering their practical use together with the OBD detector, doubling the resonant frequency to ∼2.4 MHz in water seems to be the upper resonant frequency limit, provided the cantilever compliance is not sacrificed. Thus, the upper limit of the imaging rate is approximately 40 fps under the same condition as above.

6.2. Scanner

The maximum scan range of a scanner employed in the current high-speed AFM apparatus is limited to 1–4 μm in the x and y directions and ∼1 μm in the z direction. The scan range in the x and y directions has to be increased at least ten-times and that in the z direction has to be increased >5 times for imaging cells. As a matter of course, the highest possible imaging rate is reduced. However, the reduction in the speed of x-scanning may not be so significant because the bandwidth of the x-scanner can be increased by an inverse compensation method [7]. After slowly imaging a whole cell surface, a selected small area of the cell surface can be imaged quickly using the same scanner. This imaging can be done for bacterial cells but not for mammalian cells because mammalian cells are extremely soft.

6.3. Next generation of high-speed AFM

6.3.1. High-speed diaphano-AFM. An exciting report was published in *Science* in 2005 by Shekhawat and Dravid [189]. They developed scanning near-field ultrasound holography (SNFUH) for high-resolution sub-surface imaging in air. They presented sub-surface images such as gold nanoparticles embedded in a polymer film, voids embedded in polymer coatings over nitride trench walls and malaria in red blood cells. A high-frequency acoustic wave (frequency f_1) is launched from under the sample stage, and this wave then propagates through the sample. The propagated ultrasound can be detected by the tip as well as by the lever of a cantilever with a resonant frequency of f_c. To ensure the near-field detection by the tip and hence high resolution, another acoustic wave with a frequency f_2 ($|f_1 - f_2| \sim f_c$) is launched from the cantilever base so that nonlinear tip–sample interaction generates an acoustic wave with a frequency $|f_1 - f_2|$ and therefore the cantilever is efficiently excited by the generated acoustic wave. According to their interpretation for the sub-surface imaging, materials embedded in the sample with different elastic modulus/density ratios modulate the phase and amplitude of the propagating acoustic wave, and hence the cantilever tip detecting the acoustic wave senses the embedded materials. However, it is very likely that embedded materials affect the elasticity of the sample surface and this effect seems to be detected by the cantilever tip. In fact, when materials are embedded deeply from the sample surface (>1 μm; much shorter than the wavelength of ultrasound with a few MHz frequency), no sub-surface image appears in the acoustic phase image (unpublished data). It has been demonstrated that SNFUH has a capability of imaging artificial solid particles introduced in cells [190]. However, the live cell membranes are extremely soft and therefore it is likely that the cantilever tip deeply pushes the cell membrane to sense the solid particles.

Because of this likely indirect detection of shallowly embedded materials in the contact mode, SNFUH will not be widely used to image intracellular structures. Alternative techniques need to be developed to materialize a true imaging of the interior of live cells at high resolution. One possibility is to increase the spatial resolution of scanning acoustic microscopy (SAM) that can image the interior of cells with low resolution (∼ a few micrometers), under the non-contact condition [191]. Once an operational principle for high-resolution and high-contrast detection of acoustic waves in SAM is established, it will open up an avenue to materialize high-speed diaphano-AFM not for observing individual molecules but for observing intracellular organelles and cytoskeletons in live cells. The non-contact condition can remove feedback operation and thus will make ultrafast imaging possible. We are currently attempting to find a way to enable high-resolution and high-contrast detection of acoustic waves in SAM.

6.3.2. Non-contact high-speed AFM. As mentioned above, mammalian cells are extremely soft, so that they are largely deformed by the contact with a cantilever tip before detectable cantilever deflection appears. Therefore, interesting dynamic molecular processes occurring on the live cell surface cannot be imaged except for small cellular structures such as dendritic spines. Thus far, a true non-contact condition is only achieved under vacuum environments using frequency-modulation (FM) AFM [192, 193]. In liquids FM–AFM has been used but can only operate in the brief contact condition. In addition, the oscillation amplitude of

a cantilever has to be $\lesssim$0.2 nm to achieve high detection sensitivity of the tip–sample interaction, inapplicable to a surface with large corrugations.

When the sample stage is vibrated in the z direction at a high frequency, with small amplitude, this vibration transmits to the solution placed on the stage. This transmission pattern may depend on the sample and therefore the sample may be able to be detected by a cantilever. However, even in the near-field regime, both tip and lever of the cantilever sense the water vibrations. The lever senses more efficiently than the tip. The tip is aligned in parallel to the direction in which the vibration transmits, leading to low sensitivity. Thus, this approach will not grant single-nanometer resolution in the lateral direction.

The non-contact imaging capability in liquids has already been achieved by ion-conductance scanning probe microscopy (ICSPM) [194]. Owing to the progress in fabrication techniques for producing very sharp glass capillaries with a small pore at the apex, the spatial resolution of ICSPM has reached a few nanometers [195]. Immobile protein molecules with a size of ∼14 nm on living cell membranes have been successfully imaged [196]. However, it seems difficult to increase the imaging rate of ICSPM; the bandwidth of ion-conductance detection cannot easily be increased, because of the high impedance to ionic current through the small pore of the capillary electrode.

Thus far, there are no potential methods to visualize dynamic molecular events on extremely soft mammalian cell surfaces. An alternative and compromising way may be to attach live cells with a thin film having small pores of ∼100 nm diameter. Cell surfaces exposed to the pores are rigid and therefore can be imaged.

7. Conclusion

To directly observe biological molecules at work was a holy grail in biology. Efforts over the last two decades at last materialized this long-quested dream. In high-resolution AFM movies, we can see how molecules are dynamically behaving, changing their structure and interacting with other molecules, and hence we can quickly understand in stunning detail how molecules operate to function. This new approach will spread over the world and widely applied to a vast array of biological issues, leading to a number of new discoveries. The extension of high-speed AFM to a tool for imaging live cells, which allows direct *in situ* observation of dynamic processes of molecules and organelles, remains an exciting challenge but will be made in the near future because it is a right and fruitful goal.

Acknowledgments

I would like to thank T Uchihashi, N Kodera, M Shibata, D Yamamoto, H Yamashita, H Kandori and previous many students in my lab for collaborations and discussions on interesting topics I described in this review. Without their dedication, high-speed bio-AFM would not have been materialized. I would also like to thank the members of the high-speed bio-AFM consortium, P Hinterdorfer, S Scheuring, P-E Milhiet, Ch Le Grimellec, E Lesniewska and Y Lyubchenko, for shearing ideas and scientific interests. Long-term financial support by NEDO, JST, MEXT, Knowledge Cluster Initiative and the Mitsubishi Foundation is gratefully acknowledged.

References

[1] Betzig E and Chichester R J 1993 *Science* **262** 1422
[2] Funatsu T, Harada Y, Tokunaga M, Saito K and Yanagida T 1995 *Nature* **374** 555
[3] Huang B, Bates M and Zhuang X 2009 *Annu. Rev. Biochem.* **78** 993
[4] Chapman H N *et al* 2006 *Nature Phys.* **2** 8393
[5] Vianni M B, Pietrasanta L I, Thompson J B, Chand A, Gebeshuber I C, Kindt J H, Richter M, Hansma H G and Hansma P K 2000 *Nature Struct. Biol.* **7** 644
[6] Ando T, Kodera N, Takai E, Maruyama D, Saito K and Toda A 2001 *Proc. Natl Acad. Sci. USA* **98** 12468
[7] Ando T, Uchihashi T and Fukuma T 2008 *Prog. Surf. Sci.* **83** 337
[8] Binnig G, Quate C F and Gerber Ch 1986 *Phys. Rev. Lett.* **56** 930
[9] Gould S, Marti O, Drake B, Hellemans L, Bracker C E, Hansma P K, Keder N L, Eddy M M and Stucky G D 1988 *Nature* **332** 332
[10] Marti O, Ribi H R, Drake B, Albrecht T R, Quate C F and Hansma P K 1988 *Science* **239** 50
[11] Drake B, Prater C B, Weisenhorn A L, Gould S A C, Albrecht T R, Quate C F, Cannell D S, Hansma H G and Hansma P K 1989 *Science* **243** 1586
[12] Müller D J and Dufrêne Y F 2008 *Nature Nanotechnol.* **3** 261
[13] Müller D J, Helenius J, Alsteens D and Dufrêne Y F 2009 *Nature Chem. Biol.* **5** 383
[14] Schabert F A and Engel A 1994 *Biophys. J.* **67** 2394
[15] Engel A and Müller D J 2000 *Nature Struct. Biol.* **7** 715
[16] Scheuring S and Sturgis J N 2005 *Science* **309** 484
[17] Stroh C, Wang H, Bash R, Ashcroft B, Nelson J, Gruber H, Lohr D, Lindsay S M and Hinterdorfer P 2001 *Proc. Natl Acad. Sci. USA* **101** 12503
[18] Hinterdorfer P and Dufrêne Y F 2006 *Nature Methods* **3** 347
[19] Williams P M, Fowler S B, Best R B, Toca-Herrera J L, Scott K A, Steward A and Clarke J 2003 *Nature* **422** 446
[20] Fernandez J M and Li H 2004 *Science* **303** 1674
[21] Nakajima H, Kunioka Y, Nakano K, Shimizu K, Seto M and Ando T 1997 *Biochem. Biophys. Res. Commun.* **234** 178
[22] Touhami A, Nysten B and Dufrêne Y F 2003 *Langmuir* **19** 4539
[23] Dague E, Alsteens D, Latgé J-P, Verbelen C, Raze D, Baulard A R and Dufrêne Y F 2007 *Nano Lett.* **7** 3026
[24] Binnig G, Gerber Ch, Stoll E, Albrecht T and Quate C F 1987 *Europhys. Lett.* **3** 1281
[25] Meyer G and Amer N M 1988 Novel optical approach to atomic force microscopy *Appl. Phys. Lett.* **53** 1045–947
[26] Zhong Q, Inniss D, Kjoller K and Elings V B 1993 *Surf. Sci. Lett.* **290** L688
[27] Häberle W, Höber J K H, Ohnesorge F, Smith D P E and Binnig G 1992 *Ultramicroscopy* B **42–44** 1161
[28] Ohnesorge F *et al* 1992 *Ultramicroscopy* B **42–44** 1236
[29] Bezanilla M, Drake B, Nudler E, Kashlev M, Hansma P K and Hansma H G 1994 *Biophys. J.* **67** 2454
[30] Guthold M, Bezanilla M, Erie D A, Jenkins B, Hansma H G and Bustamante C 1994 *Proc. Natl Acad. Sci. USA* **91** 12927
[31] Kasas S, Thomson N H, Smith B L, Hansma H G, Zhu X, Guthold M, Bustamante C, Kool E T, Kashlev M and Hansma P K 1997 *Biochemistry* **36** 461

[32] Guthold M, Zhu X, Rivetti C, Yang G, Thomson N H, Kasas S, Hansma H G, Smith B, Hansma P K and Bustamante C 1999 *Biophys. J.* **77** 2284
[33] Lin H, Glegg D O and Lal R 1999 *Biochemistry* **38** 9956
[34] Oberleithner H, Schillers H, Wilhelmi M, Butzke D and Danker T 2000 *Pflügers Arch.* **439** 251
[35] Radmacher M, Fritz M, Hansma H G and Hansma P K 1994 *Science* **265** 1577
[36] Thomson N H, Fritz M, Radmacher M, Cleveland J P, Schmidt C F and Hansma P K 1996 *Biophys. J.* **70** 2421
[37] Parot P, Dufrêne Y F, Hinterdorfer P, Le Grimellec Ch, Navajas D, Pellequer J-L and Scheuring S 2007 *J. Mol. Recognit.* **20** 418
[38] Ando T, Uchihashi T, Kodera N, Yamamoto D, Taniguchi M, Miyagi A and Yamashita H 2008 *Pflügers Arch.* **456** 211
[39] Barrett R C and Quate C F 1991 *J. Vac. Sci. Technol.* B **9** 302
[40] Sulchek T, Minne S C, Adams J D, Fletcher D A, Atalar A and Quate C F 1999 *Appl. Phys. Lett.* **75** 1637
[41] Rogers B, Manning L, Sulchek T and Adams J D 2004 *Ultramicroscopy* **100** 267
[42] Minne S C, Yaralioglu G, Manalis S R, Adams J D, Zesch J, Atalar A and Quate C F 1998 *Appl. Phys. Lett.* **72** 2340–2
[43] Minne S C, Adames J D, Yaralioglu G, Manalis S R, Atalar A and Quate C F 1998 *Appl. Phys. Lett.* **73** 1742
[44] Sulchek T, Grow R J, Yaralioglu G G, Minne S C, Quate C F, Manalis S R, Kiraz A, Aydine A and Atalar A 2001 *Appl. Phys. Lett.* **78** 1787
[45] Rogers B *et al* 2003 *Rev. Sci. Instrum.* **74** 4683
[46] Walters D A, Cleveland J P, Thomson N H and Hansma P K 1996 *Rev. Sci. Instrum.* **67** 3583
[47] Schäffer T E, Cleveland J P, Ohnesorge F, Walters D A and Hansma P K 1996 *J. Appl. Phys.* **80** 3622
[48] Viani M B, Schäffer T E, Chand A, Rief M, Gaub H E and Hansma P K 1999 *J. Appl. Phys.* **86** 2258
[49] Viani M B *et al* 1999 *Rev. Sci. Instrum.* **70** 4300
[50] Ando T, Kodera N, Maruyama D, Takai E, Saito K and Toda A 2002 *Japan. J. Appl. Phys.* **41** 4851
[51] Kodera N, Yamashita H and Ando T 2005 *Rev. Sci. Instrum.* **76** 053708
[52] Kodera N, Sakashita M and Ando T 2006 *Rev. Sci. Instrum.* **77** 083704
[53] Uchihashi T, Yamashita H and Ando T 2006 *Appl. Phys. Lett.* **89** 213112
[54] Fantner G E, Hegarty P, Kindt J H, Schitter G, Cidade G A G and Hansma P K 2005 *Rev. Sci. Insturm.* **76** 026118
[55] Fantner G E *et al* 2006 *Ultramicroscopy* **106** 881
[56] Kindt J H, Fantner G E, Cutroni J A and Hansma P K 2004 *Ultramicroscopy* **100** 259
[57] Humphris A D L, Miles M J and Hobbs J K 2005 *Appl. Phys. Lett.* **86** 034106
[58] Picco L M, Bozec L, Ulcinas A, Engledew D J, Antognozzi M, Horton M A and Miles M J 2007 *Nanotechnology* **18** 044030
[59] Schitter G and Phan N 2008 *Proc. Am. Control Conf. (Seattle, WA, June 2008)* pp 2690–5
[60] Kitazawa M, Shiotani K and Toda A 2003 *Japan. J. Appl. Phys.* **42** 4844
[61] Ando T and Uchihashi T 2011 *Nanoscale Liquid Interfaces: Wetting Patterning and Force Microscopy at Molecular Scale* ed T Ondarçuhu and J-P Aimé (Singapore: Pan Stanford, CA) in press
[62] Ando T, Uchihashi T, Kodera N, Miyagi A, Nakakita R, Yamashita H and Matada K 2005 *J. Surf. Sci. Nanotechnol.* **3** 384
[63] Fukuma T, Okazaki Y, Kodera N, Uchihashi T and Ando T 2008 *Appl. Phys. Lett.* **92** 243119
[64] Anczykowski B, Cleveland J P, Kruger D, Elings V and Fuchs H 1998 *Appl. Phys.* A **66** 885
[65] Sulchek T, Hsieh R, Adams J D, Yaralioglu G G, Minne S C, Quate C F, Cleveland J P, Atalar A and Adderton D M 2000 *Appl. Phys. Lett.* **76** 1473
[66] Schiener J, Witt S, Stark M and Guckenberger R 2004 *Rev. Sci. Instrum.* **75** 2564
[67] Ando T, Kodera N, Naito Y, Kinoshita T, Furuta K and Toyoshima Y Y 2003 *ChemPhysChem* **4** 1196
[68] Hobbs J K, Vasileva C and Humphris A D L 2005 *Polymer* **46** 10226
[69] Ando T, Uchihashi T, Kodera N, Miyagi A, Nakakita R, Yamashita H and Sakashita M 2006 *Japan. J. Appl. Phys.* **45** 1897
[70] Yokokawa M, Wada C, Sakai T N, Yagi A, Yoshimura S H and Takeyasu K 2006 *EMBO J.* **25** 4567
[71] Yokokawa M, Yoshimura S H, Naito Y, Ando T, Yagi A, Sakai N and Takeyasu K 2006 *IEE Proc. Nanobiotechnol.* **153** 60
[72] Ulcinas A, Butler M F, Heppenstall-Butler M, Singleton S and Miles M J 2007 *J. Cryst. Growth* **307** 378
[73] Shinohara K, Kodera N and Ando T 2007 *Chem. Lett.* **36** 1378
[74] Crampton N, Yokokawa M, Dryden D T F, Edwardson J M, Rao D N, Takeyasu K, Yshimura S H and Henderson R M 2007 *Proc. Natl Acad. Sci. USA* **104** 12755
[75] Kobayashi M, Sumitomo K and Torimitsu K 2007 *Ultramicroscopy* **107** 184–90
[76] Yamamoto D, Uchihashi T, Kodera N and Ando T 2008 *Nanotechnology* **19** 384009
[77] Miyagi A, Tsunaka Y, Uchihashi T, Mayanagi K, Hirose S, Morikawa K and Ando T 2008 *ChemPhysChem* **9** 1859
[78] Picco L M, Dunton P G, Ulcinas A, Engledew D J, Hoshi O, Ushiki T and Miles M J 2008 *Nanotechnology* **19** 384018
[79] Sugasawa H, Sugiyama Y, Morii T and Okada T 2008 *Japan. J. Appl. Phys.* **47** 6168
[80] Shinozaki Y, Siitonen A M, Sumitomo K, Furukawa K and Torimitsu K 2008 *Japan. J. Appl. Phy* s. **47** 6164
[81] Yamashita H, Voïtchovsky K, Uchihashi T, Antoranz Contera S, Ryan J F and Ando T 2009 *J. Struct. Biol.* **167** 153
[82] Yamamoto D, Nagura N, Omote S, Taniguchi M and Ando T 2009 *Biophys. J.* **97** 2358
[83] Igarashi K, Koivula A, Wada M, Kimura S, Penttilä M and Samejima M 2009 *J. Biol. Chem.* **284** 36186
[84] Gilmore J L, Suzuki Y, Tamulaitis G, Siksnys V, Takeyasu K and Lyubchenko Y L 2009 *Biochemistry* **48** 10492
[85] Vicary J A and Miles M J 2009 *Nanotechnology* **20** 095302
[86] Casuso I, Kodera N, Le Grimellec Ch, Ando T and Scheuring S 2009 *Biophys J.* **97** 1354
[87] Shinohara K, Kodera N and Ando T 2009 *Chem. Lett.* **38** 690
[88] Endo M and Sugiyama H 2009 *Nucleic Acids Symp. Ser.* **53** 81
[89] Endo M, Hidaka K, Kato T, Namba K and Sugiyama H 2009 *J. Am. Chem. Soc.* **131** 15570
[90] Shinozaki Y, Sumitomo K, Tsuda M, Koizumu S, Inoue K and Torimitsu K 2009 *PLoS Biol.* **7** e1000103
[91] Kodera N, Yamamoto D, Ishikawa R and Ando T 2010 *Nature* **468** 72
[92] Shibata M, Yamashita H, Uchihashi T, Kandori H and Ando T 2010 *Nature Nanotechnol.* **5** 208
[93] Yamamoto D, Uchihashi T, Kodera N, Yamashita H, Nishikori S, Ogura T, Shibata M and Ando T 2010 *Methods Enzymol.* **475** 541
[94] Yamamoto D, Taoka A, Uchihashi T, Sasaki H, Watanabe H, Ando T and Fukumori Y 2010 *Proc. Natl Acad. Sci. USA* **107** 9382
[95] Fantner G E, Barbero R J, Gray D S and Belcher A M 2010 *Nature Nanotechnol.* **5** 280–5

[96] Itani T and Santillan J J 2010 *J. Photopolym. Sci. Technol.* **23** 639
[97] Itani T and Santillan J J 2010 *Appl. Phys. Express* **3** 061601
[98] Giocondi M-C, Yamamoto D, Lesniewska E, Milhiet P E, Ando T and Le Grimellec Ch 2010 *Biochim. Biophys. Acta—Biomembranes* **1978** 703
[99] Milhiet P E, Yamamoto D, Berthoumieu O, Dosset P, Le Grimellec Ch, Verdier J-M, Marchal S and Ando T 2010 *PLos ONE* **5** e13240
[100] Sugimoto S, Yamanaka K, Nishikori S, Miyagi A, Ando T and Ogura T 2010 *J. Biol. Chem.* **285** 6648
[101] Casuso I, Sens P, Rico F and Scheuring S 2010 *Biophys. J.* **99** L47
[102] Shinohara K, Kodera N and Oohashi T 2010 *J. Polym. Sci.* A **48** 4103
[103] Endo M, Katsuda Y, Hidaka K and Sugiyama H 2010 *Angew. Chem. Int. Ed.* **49** 9412
[104] Endo M, Katsuda Y, Hidaka K and Sugiyama H 2010 *J. Am. Chem. Soc.* **132** 1592
[105] Sannohe Y, Endo M, Katsuda Y, Hidaka K and Sugiyama H 2010 *J. Am. Chem. Soc.* **132** 16311
[106] Endo M, Sugita T, Katsuda Y, Hidaka K and Sugiyam H 2010 *Chem. Eur. J.* **16** 5362
[107] Rajendran A, Endo M, Katsuda Y, Hidaka K and Sugiyama H 2010 *ACS Nano* **5** 665
[108] Suzuki Y, Higuchi Y, Hizume K, Yokokawa M, Yoshimura S H, Yoshikawa K and Takeyasu K 2010 *Ultramicroscopy* **110** 682
[109] Yokokawa M, Carnally S M, Henderson R M, Takeyasu K and Edwardson J M 2010 *FEBS Lett.* **584** 3107
[110] Tanaka F, Mochizuki T, Liang X, Asanuma H, Tanaka S, Suzuki K, Kitamura S, Nishikawa A, Ui-Tei K and Hagiya M 2010 *Nano Lett.* **10** 3560
[111] Shinozaki Y, Sumitomo K, Furukawa K, Miyashita H, Tamba Y, Kasai N, Nakashima H and Torimitsu K 2010 *Appl. Phys. Express* **3** 027002
[112] Inoue S, Uchihashi T, Yamamoto D and Ando T 2011 *Chem. Commun.* **47** 4974
[113] Shibata M, Uchihashi T, Yamashita H, Kandori H and Ando T 2011 *Angew. Chem. Int. Ed.* **50** 4410
[114] Uchihashi T, Iino R, Ando T and Noji H 2011 *Science* **333** 755
[115] Igarashi K, Uchihashi T, Koivula A, Wada M, Kimura S, Okamoto T, Penttilä M, Ando T and Samejima M 2011 *Science* **333** 1279
[116] Suzuki A, Hori T, Nishino T, Usukura J, Miyagi A, Morikawa K and Fukagawa T 2011 *J. Cell Biol.* **193** 125
[117] Endo M, Hidaka K and Sugiyama H 2100 *Org. Biomol. Chem.* **9** 2075
[118] Wickham S F J, Endo M, Katsuda Y, Hidaka K, Bath J, Sugiyama H and Turberfield A J 2011 *Nature Nanotechnol.* **6** 166
[119] Yamamoto S-I, Okada T, Uraoka Y, Yamashita I and Hasegawa S 2011 *J. Appl. Phys.* **109** 034901
[120] Yifrach O and Horovitz A 1994 *J. Mol. Biol.* **243** 397
[121] Schmidt M, Rutkat K, Rachel R, Pfeifer G, Jaenicke R, Viitanen P, Lorimer G and Buchner J 1994 *Science* **265** 656
[122] Halford S E, Welsh A J and Szczelkun M D 2004 *Annu. Rev. Biophys. Biomol. Struct.* **33** 1
[123] Sears A, Peakman L J, Wilson G G and Szczelkun M D 2005 *Nucleic Acids Res.* **33** 4775
[124] Ramanathan Sp, van Aelst K, Sears A, Pekman L J, Diffin F M, Szczelkun M D and Seidel R 2009 *Proc. Natl Acad. Sci. USA* **106** 1748
[125] Dryden D T F, Edwardson J M and Henderson R M 2011 *Nucleic Acids Res.* **39** 4525
[126] Masuda M and Shimizu T 2004 *Langmuir* **20** 5969
[127] Roux A, Cuvelier D, Nassoy P, Prost J, Bassereau P and Goud B 2005 *EMBO J.* **24** 1537
[128] Ellis M J and Hebert H 2001 *Micron* **32** 541
[129] Reviakine I, Bergsma-Schutter W and Brisson A 1998 *J. Struct. Biol.* **121** 356
[130] Wang S W, Robertson C R and Gast A P 1999 *Langmuire* **15** 1541
[131] Müller D J, Heymann J B, Oesterhelt F, Möller C, Gaub H, Büldt G and Engel A 2000 *Biochim. Biophys. Acta* **1460** 27
[132] Müller D J, Sass H-J, Müller S A, Büldt G and Engel A 1999 *J. Mol. Biol.* **285** 1903
[133] Haupts U, Tittor J and Oesterhelt D 1999 *Annu. Rev. Biophys. Biomol. Struct.* **28** 367
[134] Lanyi J K 2004 *Annu. Rev. Physiol.* **66** 665
[135] Kimura Y, Vassylyev D G, Miyazawa A, Kidera A, Matsushima M, Mitsuoka K, Murata K, Hirai T and Fujiyoshi Y 1997 *Nature* **389** 206
[136] Luecke H, Schobert B, Richter H T, Cartailler J P and Lanyi J K 1999 *J. Mol. Biol.* **291** 899
[137] Luecke H, Schobert B, Lanyi J K, Spudich E N and Spudich J L 2001 *Science* **293** 1499
[138] Sass H J, Buldt G, Gessenich R, Hen D, Neff D, Schleisinger R, Berendzen J and Ormos P 2000 *Nature* **406** 649
[139] Subramaniam S and Henderson R 2000 *Nature* **406** 653
[140] Otto H, Marti T, Holz M, Mogi T, Lindau M, Khorana H G and Heyn M P 1989 *Proc. Natl Acad. Sci. USA* **86** 9228
[141] Druckmann S, Friedman N, Lanyi J K, Needleman R, Ottolenghi M and Sheves M 1992 *Photochem. Photobiol.* **56** 1041
[142] Duque D, Li X J, Katsov K and Schick M 2002 *J. Chem. Phys.* **116** 10478
[143] Phillips R, Ursell T, Wiggins P and Sens P 2009 *Nature* **459** 379
[144] Ihara K, Abe T, Sugimura K and Mukohata Y 1992 *J. Exp. Biol.* **172** 475
[145] Dunker A K, Brown C J, Lawson J D, Lakoucheva L M and Obradovic Z 2002 *Biochemistry* **41** 6573
[146] Dyson H J and Wright P E 2005 *Nature Rev. Mol. Cell Biol.* **6** 197
[147] Belotserkovskaya R, Oh S, Bondarenko V A, Orphanides G, Studitsky V M and Reinberg D 2003 *Science* **301** 1090
[148] Shimojima T, Okada M, Nakayama T, Ueda H, Okawa K, Iwamatsu A, Handa H and Hirose S 2003 *Genes Dev.* **17** 1605
[149] Rivetti C, Guthold M and Bustamante C 1996 *J. Mol. Biol.* **264** 919
[150] Dietz H and Rief M 2004 *Proc. Natl Acad. Sci. USA* **101** 16192
[151] Li H, Oberhauser A F, Redick S D, Carrion-Vazquez M, Erickson H P and Fernandez J M 2001 *Proc. Natl Acad. Sci. USA* **98** 10682
[152] Smith S B, Cui Y and Bustamante C 1996 *Science* **271** 795
[153] Smith S B, Finzi L and Bustamante C 1992 *Science* **258** 1122
[154] Müller D J, Baumeister W and Engel A 1999 *Proc. Natl Acad. Sci. USA* **96** 13170
[155] Sellers J R and Weisman L S 2008 *A Superfamily of Molecular Motors, Proteins and Cell Regulation* ed L Coluccio (Berlin: Springer) p 289
[156] Mehta A D, Rock R S, Rief M, Spudich J A, Mooseker M S and Cheney R E 1999 *Nature* **400** 590
[157] Sakamoto T, Amitani I, Yokota E and Ando T 2000 *Biochem. Biophys. Res. Commun.* **272** 86
[158] Yildiz A, Forkey J N, McKinney S A, Ha T, Goldman Y E and Selvin P R 2003 *Science* **300** 2061
[159] Forkey J N, Quinlan M E, Shaw M A, Corrie J E T and Goldman Y E 2003 *Nature* **422** 399

[160] Sakamoto T, Webb M R, Forgacs E, White H D and Sellers J R 2008 *Nature* **455** 128
[161] De La Cruz E M, Wells A L, Rosenfeld S S, Ostap E M and Sweeney H L 1999 *Proc. Natl Acad. Sci. USA* **96** 13726
[162] Wells A L, Lin A W, Chen L Q, Safer D, Cain S M, Hasson T, Carragher B O, Milligan R A and Sweeney H L 1999 *Nature* **401** 505
[163] Huxley H E 1969 *Science* **164** 1356
[164] Rosenfeld S S and Sweeney H L 2004 *J. Biol. Chem.* **279** 40100
[165] Veigel C, Schmitz S, Wang F and Sellers J R 2005 *Nature Cell Biol.* **7** 861
[166] Purcell T J, Sweeney H L and Spudich J A 2005 *Proc. Natl Acad. Sci. USA* **102** 13873
[167] Teeri T T 1997 *Trends Biotechnol.* **15** 160
[168] Teeri T T, Koivula A, Linder M, Wohlfahrt G, Divne C and Jones T A 1998 *Biochem. Soc. Trans.* **26** 173
[169] Divne C, Stahlberg J, Reinikainen T, Ruohonen L, Pettersson G, Knowles J K, Teeri T T and Jones T A 1994 *Science* **265** 524
[170] Kipper K, Väljamäe P and Johansson G 2005 *Biochem. J.* **385** 527
[171] Khakh B S and North R A 2006 *Nature* **442** 527
[172] North R A 2002 *Physiol. Rev.* **82** 1013
[173] Kawate T, Michel J C, Birdsong W T and Gouaux E 2009 *Nature* **460** 592
[174] Khakh B S, Bao X R, Labarca C and Lester H A 1999 *Nature Neurosci.* **2** 322
[175] Pepys M B 2006 *Annu. Rev. Med.* **57** 223
[176] Ohnishia S and Takanobu K 2004 *Cell. Mol. Life Sci.* **61** 511
[177] Gerbaud V, Pignol D, Loret E, Bertrand J A, Berland Y, Fontecilla-Camps J C, Canselier J P, Gabas N and Verdier J M 2000 *J. Biol. Chem.* **275** 1057
[178] Lee B I, Mustafi D, Cho W and Nakagawa Y 2003 *J. Biol. Inorg. Chem.* **8** 341
[179] De Caro A, Lohse J and Sarles H 1979 *Biochem. Biophys. Res. Commun.* **87** 1176
[180] Sekikawa A *et al* 2005 *Gut* **54** 1437
[181] Cerini C *et al* 1999 *J. Biol. Chem.* **274** 22266
[182] Laurine E *et al* 2003 *J. Biol. Chem.* **278** 51770
[183] Grégoire C, Marco S, Thimonier J, Duplan L, Laurine E, Chauvin J-P, Michel B, Peyrot V and Verdier J-M 2001 *EMBO J.* **20** 3313
[184] Seeman N C 2003 *Nature* **421** 427
[185] Tian Y, He Y, Peng Y and Mao C 2005 *Angew. Chem. Int. Edn* **44** 4355
[186] Bath J, Green S J and Turberfield A J 2005 *Angew. Chem. Int. Edn* **44** 4358
[187] Fujiwara I, Takahashi S, Tadakuma H, Funatsu T and Ishiwata S 2002 *Nature Cell Biol.* **4** 666
[188] Kuhn J R and Pollard T D 2005 *Biophys. J.* **88** 1387
[189] Shekhawat G and Dravid V P 2005 *Science* **310** 89
[190] Tetard L, Passian A, Venmar K T, Lynch R M, Voy B H, Shekhawat G, Dravid V P and Thundat T 2008 *Nature Nanotechnol.* **3** 501
[191] Hilderbrand J A, Rugar D, Johnston R N and Quate C F 1981 *Proc. Natl Acad. Sci. USA* **78** 1656
[192] Albrecht T R, Grütter P, Horne D and Rugar D 1991 *J. Appl. Phys.* **69** 668
[193] Giessibl F J 1995 *Science* **267** 68
[194] Hansma P K, Drake B, Marti O, Gould S A and Prater C B 1989 *Science* **243** 641
[195] Ying L, Bruckbauer A, Zhou D, Gorelik J, Shevchuk A, Lab M, Korchev Y and Klenerman D 2005 *Phys. Chem. Chem. Phys.* **7** 2859
[196] Shevchuk A I, Frolenkov G I, Sanchez D, James P S, Freedman N, Lab M J, Jones R, Klenerman D and Korchev Y E 2006 *Angew. Chem. Int. Edn* **45** 2212